
SPACE: Unifying Symmetric and Asymmetric Routing Problems for Generalist Neural Solver

Rongsheng Chen^{1,2,3} Changliang Zhou^{1,3} Canhong Yu⁴ Yuanyao Chen^{1,3}
 Yu Zhou⁴ Zhuo Chen² Zhenkun Wang^{1,3}

¹ School of Automation and Intelligent Manufacturing,
 Southern University of Science and Technology, Shenzhen, China

² Pengcheng Laboratory, Shenzhen, China

³ Guangdong Provincial Key Laboratory of Fully Actuated System Control Theory and Technology,
 Southern University of Science and Technology, Shenzhen, China

⁴ College of Computer Science and Software Engineering, Shenzhen University, Shenzhen, China
 {chenrs2025,zhouc12022}@mail.sustech.edu.cn, 2410103054@mails.szu.edu.cn,
 12433020@mail.sustech.edu.cn, zhouyu_1022@126.com, chenzhuo.zoom@gmail.com,
 wangzk3@sustech.edu.cn

Abstract

Generalist neural routing solvers have shown great potential in solving diverse vehicle routing problems (VRPs) with a unified model. However, existing solvers are typically limited to symmetric settings or degrade in performance when switching to asymmetric settings due to input inconsistencies or inherent structural differences, substantially limiting their practicality in real-world scenarios that encompass both scenarios. To address this limitation, we define the spatial position of each node based on the relative distances to a specific set of pivots and further propose a Spatial Pivot-Aligned Coordinate-free Embedding (SPACE) framework that unifies node representation and solution generation across symmetric and asymmetric VRPs. Specifically, we construct a bidirectional Fréchet representation using a novel furthest pivot sampling strategy to enable invariant node representations across distinct problem settings. Furthermore, we introduce a weight-decomposed adaptive decoding mechanism that decouples geometric perception from problem representations, mitigating the overfitting of constraint decisions to a specific geometry setting. Extensive experiments on 110 VRP variants, comprising 55 symmetric problems and their asymmetric counterparts, demonstrate that SPACE achieves promising zero-shot generalization in both symmetric and asymmetric VRPs.

1 Introduction

The Vehicle Routing Problem (VRP) is an essential class of combinatorial optimization problems (COPs) and has significant practical importance in domains such as logistics and supply chain management [1]. As an NP-hard problem, solving diverse VRPs efficiently is challenging. While exact solvers guarantee optimality, their prohibitive computational costs render them impractical for real-world scenarios. In contrast, traditional heuristics [2, 3] have achieved remarkable performance within reasonable time limits over the past few decades. However, these methods rely heavily on extensive domain expertise to handcraft specialized rules for specific problems. Given the rapidly growing diversity of VRP variants in practical applications, manual adjustment for each case has become increasingly impractical.

Recently, neural combinatorial optimization (NCO) methods have attracted significant attention for their potential to reduce reliance on expert knowledge while maintaining competitive solution quality [4, 5]. By automatically learning implicit heuristic rules from data, numerous specialist

solvers achieve promising performance on specific problems like the Traveling Salesman Problem (TSP) [6, 7] and the Capacitated VRP (CVRP) [8, 9]. However, they typically require per-problem retraining to accommodate the specific constraints and attributes of distinct VRP variants. More critically, most methods focus on symmetric settings and heavily rely on coordinate-based encoding schemes, rendering them inapplicable to asymmetric settings where node coordinates are unavailable. These limitations impose substantial training overhead and hinder practical deployment on new problems, especially in asymmetric scenarios.

To address the challenge of cross-problem generalization, research focus has increasingly shifted toward generalist neural routing solvers capable of handling diverse VRP variants. Existing efforts can be broadly categorized into three paradigms: 1) constraint combination; 2) adapter-based fine-tuning; and 3) the emerging unified data representation. The first category treats VRP variants as combinations of predefined constraints and trains a unified model across these combinations to enable knowledge sharing among seen constraints [10, 11]. The second approach builds a shared backbone for all problems while incorporating problem-specific input/output adapters, thereby reducing retraining costs [12, 13]. The last paradigm replaces problem enumeration with data unification, significantly broadening the problem coverage to over 100 VRP variants [14]. A detailed review of related work on specialist and generalist neural solvers is provided in Appendix A.

Despite these advancements, existing methods still suffer from limited applicability, as most generalist solvers remain limited in symmetric VRPs. However, real-world scenarios encompass both symmetric and asymmetric settings. For instance, while drone route planning typically operates in symmetric settings [15], urban express delivery often exhibits significant asymmetry [16]. This duality necessitates a unified solver that seamlessly handles both settings to effectively address complex real-world challenges. As illustrated in Figure 1,

although URS [14] and GOAL [13] have attempted to address this challenge, they exhibit notable drawbacks. URS relies on distinct positional representations for these two settings, hindering the sharing of learned structural knowledge and compromising its zero-shot generalization on asymmetric variants. Conversely, while the adapter-based GOAL employs a unified distance-only encoding, the inherent structural difference results in performance degradation when switching between distinct settings. In addition, GOAL lacks zero-shot generalization capabilities for unseen problem variants.

In this paper, grounded in Bourgain’s Theorem [17], we construct an invariant node representation for unifying symmetric and asymmetric VRPs. By defining the spatial position of each node based on its distances to a specific set of **pivots**, we propose a **S**patial **P**ivot-**A**ligned **C**oordinate-free **E**mbedding (SPACE) framework, which significantly improves cross-problem zero-shot generalization for NCO methods, especially in asymmetric VRPs. Our contributions can be summarized as follows:

- We construct a bidirectional Fréchet representation using a novel furthest pivot sampling strategy. It enables a unified node representation across symmetric and asymmetric VRPs, thereby delivering superior results across both symmetric and asymmetric variants.
- We introduce a weight-decomposed adaptive decoding mechanism that decouples geometric perception from problem representations, mitigating the overfitting of constraint decisions to a specific geometry setting.

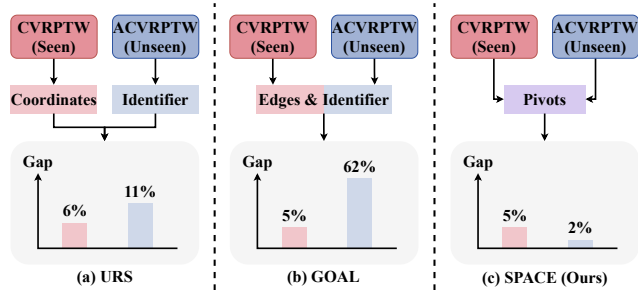


Figure 1: **Effects of node representations on generalization gaps across different generalist solvers.** Both (a) URS [14] and (b) GOAL [13] suffer from performance degradation caused by input inconsistencies or inherent structural differences between symmetric and asymmetric settings. (c) Our SPACE employs an invariant node representation to unify two problem settings, ensuring robust zero-shot generalization.¹

¹Given that GOAL already captures both symmetric and asymmetric features during training, we adopt an adapter sharing strategy to minimize retraining costs.

- Extensive experiments on **110** VRP variants, comprising 55 symmetric problems and their asymmetric counterparts, demonstrate that SPACE achieves promising zero-shot generalization in both symmetric and asymmetric VRPs.

2 Background and Motivation

In this section, we first formulate VRPs and then review the common pipeline of autoregressive constructive solvers. Finally, based on our preliminary experiment and theoretical analysis, we identify a potential limitation in current encoding and introduce a targeted technique to address it.

2.1 Vehicle Routing Problems

Mathematically, the VRP is formulated as an optimization task within a finite action space. Formally, an instance is a tuple $\mathcal{G} = (\mathcal{V}, \mathbf{D})$, where $\mathcal{V} = \{v_i\}_{i=0}^n$ denotes the set of $n + 1$ nodes unless the variant has no depot (e.g., TSP). In VRP, each node $v_i \in \mathcal{V}$ indicates node coordinates $\{x_i, y_i\}$ when available and problem-specific attributes (e.g., demands in CVRP). The edge set of the problem is characterized by $\mathbf{D} = \{d(v_i, v_j) \mid \forall i, j \in 0, 1, \dots, n\}$. To accommodate the realistic asymmetric setting, i.e., $d(v_i, v_j) \neq d(v_j, v_i)$, \mathbf{D} is characterized as a **quasimetric space**² [18], which satisfies non-negativity, identity of indiscernibles, and the triangle inequality $d(v_i, v_j) \leq d(v_i, v_k) + d(v_k, v_j)$.

A feasible solution is a set of routes that satisfies all operational constraints, where each route originates and terminates at the depot (or starting node) [19]. We represent the solution as a sequence $\pi = (\pi_1, \pi_2, \dots, \pi_T)$ (i.e., a finite sequence), which is a permutation of T nodes. The objective is to find a permutation $\pi^* \in \pi_{\text{feasible}}$ that minimizes the cost function \mathcal{J} , i.e., $\pi^* = \arg \min_{\pi \in \pi_{\text{feasible}}} \mathcal{J}(\pi | \mathcal{G})$. The function \mathcal{J} formulates diverse routing objectives. In most VRP variants, it can be represented as the cumulative distance $\sum_{i=1}^{T-1} d(\pi_i, \pi_{i+1}) + d(\pi_T, \pi_1)$.

In this paper, we target a comprehensive coverage of symmetric and asymmetric settings. Consistent with Zhou et al. [14], each variant incorporates at least one of nine constraints to reflect diverse real-world scenarios: (1) Capacity (C); (2) Open Route (O); (3) Backhaul (B); (4) Backhaul and Priority (BP); (5) Duration Limit (L); (6) Time Windows (TW); (7) Multi-Depot (MD); (8) Prize Collecting (PC); (9) Pickup and Delivery (PD). Detailed definitions are provided in Appendix B.

2.2 Autoregressive Constructive Neural Solver

Autoregressive constructive solvers have become the dominant paradigm for solving VRPs due to their significant reduction in reliance on hand-crafted heuristics. Most constructive solvers adopt an encoder-decoder architecture parametrized by $\theta = \{\theta_{\text{enc}}, \theta_{\text{dec}}\}$ [20, 8]. Without loss of generality, we delineate the pipeline using the representative AM [21]. Given an instance \mathcal{G} , the encoder θ_{enc} transforms raw node features into advanced node embeddings $H^{(L)} = \{\mathbf{h}_i^{(L)}\}_{i=0}^n$ via linear projection and subsequent L attention layers. At decoding step t , the decoder θ_{dec} sequentially appends a node to the partial solution $\pi_{1:t-1} = (\pi_1, \pi_2, \dots, \pi_{t-1})$. This process continues until a complete solution is constructed. To ensure feasibility, a masking function \mathcal{M}_t prevents invalid selections by assigning $-\infty$ logits to nodes that are either visited or violate problem-specific constraints (e.g., capacity).

2.3 Motivation and Key Idea

Rethinking Symmetric and Asymmetric Encoding The nature of the distance matrix \mathbf{D} yields a disparity within the encoding process. In symmetric instances, node coordinates provide explicit inductive biases that can fully reflect the problem setting, with \mathbf{D} serving merely as auxiliary biases to facilitate decision-making in some works [9, 22]. Conversely, for asymmetric problems, the lack of inherent node coordinates means their geometric features are entirely determined by \mathbf{D} [23, 24]. This distinction creates a critical representation gap, hindering the generalization of neural solvers that rely on symmetric spatial priors to asymmetric scenarios.

Intuitively, since the distance matrix \mathbf{D} is shared across both symmetric and asymmetric problems, a straightforward unified strategy is to rely solely on distance-based encoding. To validate the

²A quasimetric relaxes the symmetry constraint of a standard metric, allowing for asymmetric costs where $d(v_i, v_j) \neq d(v_j, v_i)$. Please refer to Appendix C.1 for more details.

limitations of this strategy, we conduct an experiment using URS [14], which is a representative neural solver capable of zero-shot generalization across a wide range of VRP variants. Specifically, we train a variant of URS that removes the explicit node coordinates used to distinguish between symmetric and asymmetric inputs, denoted URS-Dist. This compels the model to achieve representation unification via random identifiers and intrinsic distance biases D , while keeping all other configurations unchanged to ensure a fair comparison.

As illustrated in Table 1, URS-Dist outperforms URS overall and in asymmetric VRPs, which validates the necessity of a unified representation. However, it exhibits performance degradation in symmetric variants. We attribute this to the removal of explicit coordinates, which deprives the attention [25] of essential spatial symmetry priors. Since D is used solely as a scalar attention bias, the model is forced to learn two distinct geometric spaces using the same attention without any input priors, making it challenging for the model to perform well in both symmetric and asymmetric settings. These empirical findings highlight the critical need for an advanced coordinate-free encoding scheme that provides relative spatial positions and distinguishable symmetric/asymmetric priors, thereby achieving robust zero-shot generalization across symmetric and asymmetric VRPs.

The Necessity of Bi-Lipschitz Embedding

To unify symmetric and asymmetric instances, neural solvers require a mapping $\Phi : \mathcal{V} \rightarrow \mathbb{R}^k$ that transforms discrete nodes into continuous feature vectors without discarding the geometric priors encoded by the distance matrix D . This requirement naturally motivates a Lipschitz-type stability criterion: nearby nodes in the underlying routing geometry should remain nearby in the embedding space, while excessive contraction should be avoided whenever the selected reference points sufficiently separate the nodes [17]. However, because distances induced by normed vector spaces are symmetric, whereas asymmetric costs satisfy $d(v_i, v_j) \neq d(v_j, v_i)$, a direct bi-Lipschitz condition with respect to the raw quasimetric d is mathematically inappropriate. We therefore formulate the stability target with respect to a symmetrized reference metric, and retain asymmetric information through directional reference-distance coordinates.

Formally, for a symmetric reference metric D , an embedding Φ is termed L -Lipschitz if distance expansion in the embedding space is bounded by a factor of L . If it is also non-contractive up to a constant, then Φ is a *bi-Lipschitz embedding*: there exist constants $\alpha, \beta > 0$ such that for all node pairs $v_i, v_j \in \mathcal{V}$,

$$\alpha \cdot D(v_i, v_j) \leq \|\Phi(v_i) - \Phi(v_j)\|_p \leq \beta \cdot D(v_i, v_j). \tag{1}$$

The embedding is quantified by its distortion, defined as $\mathcal{D}(\Phi) = \beta/\alpha$ [26]. If an isometric embedding achieves $\mathcal{D}(\Phi) = 1$, it represents perfect geometric preservation.

Low distortion is desirable because existing neural routing solvers [21, 8] leverage attention mechanisms [25] whose vector similarities are expected to correlate with routing costs. Excessive distortion $\mathcal{D}(\Phi)$ causes the vector-space geometry to diverge from the true costs, thereby making cost-dependent feasibility harder to infer from embeddings alone³. For the BFR used in SPACE, we only claim a provable non-expansive stability bound for arbitrary pivot sets; a lower-bound or bounded-distortion statement requires an additional pivot-separation condition, stated explicitly in Proposition C.8. We further show in Proposition C.9 that a smaller pivot covering radius improves this separation behavior.

The Feasibility of Coordinate-free Encoding

Obtaining a low-distortion embedding necessitates establishing whether the underlying geometry can be constructed solely from distance information. To this end, Bourgain’s Embedding Theorem [17] provides a fundamental guarantee: any finite metric space can be embedded into a Euclidean space with bounded distortion by defining coordinates based

Table 1: Gap comparison between different representation strategies.

Problem		URS	URS-Dist
CVRPTW	Sym.	6.13%	6.28%
	Asym.	11.28%	9.34%
	Avg.	8.71%	7.81%
OCVRPTW	Sym.	5.07%	5.25%
	Asym.	17.47%	14.24%
	Avg.	11.27%	9.74%
OCVRPBP	Sym.	14.30%	16.57%
	Asym.	28.27%	22.23%
	Avg.	21.29%	19.40%
PDTSP	Sym.	4.98%	6.09%
	Asym.	6.21%	-2.31%
	Avg.	5.60%	1.89%
PDCVRP	Sym.	-1.47%	1.43%
	Asym.	7.03%	3.55%
	Avg.	2.78%	2.49%

³We provide a formal derivation of how distortion impacts geometric constraints in Proposition C.4 (Appendix C.2).

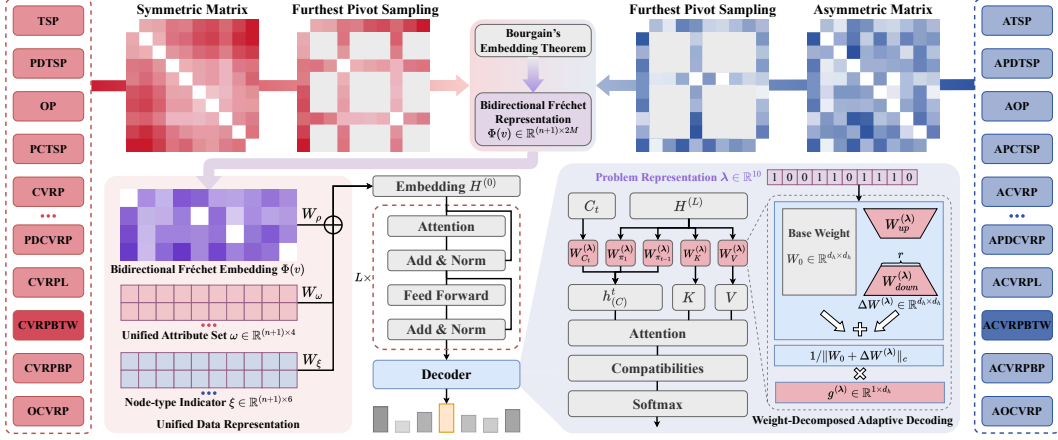


Figure 2: **Overview of our SPACE framework, illustrated on the (A)CVRPBTW instances.** By leveraging a unified bidirectional Fréchet representation coupled with a weight-decomposed adaptive decoding mechanism, SPACE achieves robust cross-problem zero-shot generalization across both symmetric and asymmetric VRPs, particularly remarkable in asymmetric scenarios.

on distances to specific subsets of nodes (pivots). The theorem ensures that there exists an embedding where distances are contracted by at most a logarithmic factor while maintaining the upper bound of the original metric (see Theorem C.5 in Appendix C.3 for the formal statement and bounds).

The embedding theorem relies on defining coordinates in terms of distances to a specific subset of \mathcal{V} . Formally, each coordinate $\phi_\tau(v)$ can be defined as the distance from node v to a subset $A_\tau \subset \mathcal{V}$, denoted as $d(v, A_\tau) = \min_{a \in A_\tau} d(v, a)$. Bourgain demonstrates that by aggregating a series of random subsets $\{A_\tau\}$ of varying cardinalities, the resulting embedding $\Phi(v)$ theoretically satisfies stated distortion bounds.

This theoretical result shows that explicit coordinates are not strictly necessary to capture problem settings. While the original theorem addresses symmetric metrics, it establishes the feasibility of a coordinate-free encoding paradigm. This motivates our design to construct data representations directly from the distance matrix D , and extends it to handle asymmetric VRPs.

3 Methodology

Building on the feasibility analysis in Section 2.3, we propose a novel SPACE framework for generalist neural routing solvers, as shown in Figure 2. Since URS [14] exhibits zero-shot generalization capability on both symmetric and asymmetric VRP variants, we adopt it as our basic model. Our SPACE includes two key components. Their implementations are detailed below.

3.1 Bidirectional Fréchet Representation

Building upon the embedding concept established by Bourgain’s Theorem, we introduce a computationally efficient construction to map the VRP instance into a unified vector space. While the theorem guarantees structural preservation for metric spaces, we adapt this distance-to-reference-set perspective to finite quasimetric space (\mathcal{V}, d) by explicitly encoding directionality. We adopt the framework of *Fréchet embeddings*, which represent the spatial position of a node via its distances to a specific set of reference nodes, termed *pivots*.

Let $\mathcal{P}_M = \{p_m\}_{m=1}^M \subset \mathcal{V}$ denote a selected subset of M pivots. In symmetric Euclidean spaces, a standard embedding $\phi(v) = [d(v, p_m)]_{m=1}^M$ can encode relative positions when the pivots separate the nodes. However, realistic routing problems frequently exhibit significant asymmetry ($d(v_i, v_j) \neq d(v_j, v_i)$). A unidirectional embedding can miss this non-commutative topology. Thus, we propose the *Bidirectional Fréchet representation*, which explicitly encodes both the outgoing and incoming distances relative to the pivot set. Formally, for any node $v \in \mathcal{V}$, the embedding $\Phi : \mathcal{V} \rightarrow \mathbb{R}^{2M}$ is defined as the concatenation of the outgoing and incoming distance vectors:

$$\Phi(v) = \frac{1}{\sqrt{2M}} \bigoplus_{m=1}^M [d(v, p_m), d(p_m, v)], \quad (2)$$

where \oplus denotes vector concatenation and the factor $\frac{1}{\sqrt{2M}}$ normalizes the energy of the embedding. This construction inherently satisfies the Lipschitz condition required for geometric stability. Since the Euclidean norm is symmetric, strictly bounding the embedding distance by an asymmetric quasimetric $d(v_i, v_j)$ is mathematically ill-posed. Instead, we establish stability with respect to the *symmetrized metric* $D_{\text{sym}}(v_i, v_j) = \max(d(v_i, v_j), d(v_j, v_i))$. For any pivot p_m , the quasimetric triangle inequality in the two directions gives $|d(v_i, p_m) - d(v_j, p_m)| \leq D_{\text{sym}}(v_i, v_j)$ and $|d(p_m, v_i) - d(p_m, v_j)| \leq D_{\text{sym}}(v_i, v_j)$. Consequently, the Euclidean distance in the embedding space is upper-bounded as:

$$\|\Phi(v_i) - \Phi(v_j)\|_2 \leq \sqrt{\sum_{m=1}^{2M} \frac{1}{2M} D_{\text{sym}}(v_i, v_j)^2} = D_{\text{sym}}(v_i, v_j). \quad (3)$$

This ensures the mapping is *1-Lipschitz* regarding the symmetrized topology, guaranteeing that nodes close in the original graph (in both directions) remain close in the embedding space. Although the embedding distance $\|\cdot\|_2$ is symmetric, the concatenation of incoming and outgoing features in Eq. 2 provides directional information from which the neural decoder can learn asymmetric costs. We provide the rigorous proof, the conditional non-contraction statement, the coverage-induced separation bound, and the necessity of this bidirectional design in Proposition C.7, Proposition C.8, Proposition C.9, and Corollary C.12 (Appendix C.4).

Geometry-Preserving Pivot Selection The representational capacity of the Bidirectional Fréchet Representation Φ depends critically on the spatial distribution of the selected pivot set \mathcal{P} . Randomization frequently clusters pivots, generating highly correlated distance features that collapse the representation’s effective dimensionality and obscure fine-grained geometric details. Maximizing the information content of the representation requires maximizing the spatial diversity of \mathcal{P} .

We therefore employ *Furthest Pivot Sampling* (FPS) to construct the pivot set. Initialized with the depot node v_0 , the algorithm iteratively selects the node p_m that maximizes the minimum distance to the set of previously chosen pivots \mathcal{P}_{m-1} :

$$p_m = \arg \max_{v \in \mathcal{V}} \min_{p \in \mathcal{P}_{m-1}} d_{\text{fps}}(v, p). \quad (4)$$

Here, we utilize the metric $d_{\text{fps}}(v_i, v_j) = \frac{1}{2}(d(v_i, v_j) + d(v_j, v_i))$ to ensure balanced coverage across the underlying topology regardless of edge directionality. This iterative maximization should be interpreted as the standard furthest-first traversal for the metric d_{fps} , rather than as an exact solution to the M -center objective. Under d_{fps} , the greedy pivot set achieves the usual 2-approximation to the optimal covering radius, with the guarantee stated in Proposition D.1. The link between pivot coverage and BFR separation is formalized in Proposition C.9. Geometrically, the procedure pushes pivots toward under-covered regions of the data topology, reducing redundant distance features and helping distinct topological regions map to distinct regions in the vector space. Consequently, the representation provides the neural model with a high-resolution triangulation of the underlying geometry. More details are provided in Appendix D.

3.2 Weight-Decomposed Adaptive Decoding

While BFR unifies the input representation, neural solvers must still learn constraint-handling logic that generalizes across diverse problem settings. A recent study [14] constructs a multi-hot problem representation λ , based on input features, and employs a problem-conditioned parameter generation mechanism. While this approach mitigates the learning burden, it suffers from a key limitation. Within λ , the spatial structures (i.e., symmetric/asymmetric) and various attributes (e.g., demand) are deeply coupled. When the same attribute appears across two spatial structures or multiple attributes are recombined into unseen variants, the previously hypernetwork-based technique risks overfitting constraint decisions to a specific metric setting, thereby delivering poor results on another setting (e.g., from symmetric to asymmetric scenarios).

Inspired by Weight-Decomposed Low-Rank Adaptation (DoRA) [27], we propose weight-decomposed adaptive decoding (WDAD) to enforce a decoupling between geometric perception and problem representations, thereby improving zero-shot generalization across asymmetric and symmetric VRPs. To align with our unified representation framework, we exclude explicit identifiers for symmetric and asymmetric properties in λ (see Appendix F for details). Each active entry of λ corresponds to a routing attribute, and WDAD composes task-specific decoder parameters from these active attributes instead of allocating separate parameters to every VRP variant. For each adaptive projection matrix in the decoder, we decompose the effective weight into a shared base weight W_0 and a representation-conditioned update $\Delta W^{(\lambda)}$:

$$W_{\text{eff}}^{(\lambda)} = W_0 + \Delta W^{(\lambda)}, \quad \Delta W^{(\lambda)} = \frac{1}{Z(\lambda)} \sum_{j:\lambda_j=1} \delta_j, \quad Z(\lambda) = \max(1, \|\lambda\|_1). \quad (5)$$

where each δ_j is an attribute-specific adapter induced by the j -th active constraint. To preserve the decoupling between update direction and magnitude, each adapter is parameterized by a DoRA-style low-rank decomposition with H independent heads for every attribute:

$$\delta_j = \sum_{\eta=1}^H g_{\eta}^{(j)} \odot \frac{W_{\text{up},\eta}^{(j)} W_{\text{down},\eta}^{(j)}}{\|W_{\text{up},\eta}^{(j)} W_{\text{down},\eta}^{(j)}\|_{\text{row}} + \epsilon}, \quad (6)$$

where $W_{\text{up},\eta}^{(j)} \in \mathbb{R}^{d_{\text{out}} \times r}$ and $W_{\text{down},\eta}^{(j)} \in \mathbb{R}^{r \times d_{\text{in}}}$ determine the update direction, while $g_{\eta}^{(j)} \in \mathbb{R}^{d_{\text{out}}}$ controls the row-wise magnitude of each output channel. Here, $\|\cdot\|_{\text{row}}$ denotes the ℓ_2 norm along the input dimension of each output row. The normalization by $Z(\lambda)$ averages nonempty active-attribute updates and falls back to the shared base decoder when no attribute is active, preventing magnitude explosion when multiple constraints coexist and allowing the decoder to compose known constraint primitives into unseen combinations. WDAR allows the shared base weight W_0 to capture general routing knowledge learned from BFR, whereas $\Delta W^{(\lambda)}$ injects only the task-specific decision logic required by the active attribute. More implementation details are provided in Appendix E.

4 Experiments

In this section, we evaluate SPACE against both classical and learning-based solvers across 110 VRPs and adopt the 100-node setting as our primary evaluation criterion. All experiments are conducted on a single NVIDIA GeForce RTX 4090 GPU (24GB of memory).

4.1 Experimental Setup

Problem Setting We adopt the unified data representation established by Zhou et al. [14] and select 12 VRPs in training to ensure comprehensive feature coverage, they are: (1) ATSP [23]; (2) TSP [21]; (3) CVRP [21]; (4) ACVRP [23, 21]; (5) Orienteering Problem (OP) [21]; (6) PCTSP [21]; (7) PDTSP [28]; (8) CVRPTW [11]; (9) OCVRP [11]; (10) CVRPB [11], (11) OCVRPTW [11], and (12) ACVRPBTW [14]. We provide a detailed discussion of problem selection in Appendix K. To demonstrate the broad applicability of SPACE, we evaluate the model on 55 symmetric problems and their asymmetric counterparts. Notably, we focus on a model’s overall performance across two settings, rather than limiting it to a single scenario. Each test dataset consists of 1,000 instances.

Model & Training Setting Regarding the proposed BFR, we set the number of pivots to $M = 8$. For the WDAD, we configure the rank to $r = 32$ and the number of heads to 3. To ensure a fair comparison, all remaining hyperparameters and training protocols strictly adhere to [14] configuration. SPACE is trained by the REINFORCE [29] algorithm, and the data is generated on the fly. Further details on model architecture and training are provided in Appendix H.

Baseline We compare SPACE with the following generalist neural routing solvers: MTPOMO [10], MVMoE/4E [11], ReLD-MTL [22], RouteFinder [30], CaDA [31]⁴, GOAL-MTL [13], and URS [14]. The oracle solvers of all evaluated problems are provided in Appendix F.

⁴Due to differing training variants and constraints, we evaluate URS against RouteFinder [30] and CaDA [31] on all shared seen and unseen VRPs under consistent problem settings (see Appendix I.2 for comparable results).

Table 2: Performance comparison on the 12 VRP variants used in SPACE training.

Method	CVRP100		ACVRP100		CVRPTW100		CVRPB100		OCVRP100		OCVRPTW100	
	Gap	Time	Gap	Time	Gap	Time	Gap	Time	Gap	Time	Gap	Time
Oracle	0.00%	9.1m	0.00%	6.6m	0.00%	19.6m	0.00%	20.8m	0.00%	5.3m	0.00%	20.8m
MVMoE	1.65%	12s	—	—	4.90%	15s	1.28%	11s	3.14%	13s	3.85%	15s
MTPOMO	1.85%	6s	—	—	5.31%	8s	1.67%	5s	3.46%	6s	4.41%	7s
ReLD-MTL	1.42%	8s	—	—	4.56%	10s	0.90%	6s	2.32%	7s	3.10%	9s
GOAL-MTL	4.22%	48s	—	—	4.66%	42s	—	—	—	—	—	—
URS	1.81%	6s	3.06%	1.4m	6.13%	8s	1.46%	6s	3.24%	6s	5.07%	8s
SPACE	1.83%	7s	2.67%	1.8m	5.36%	9s	1.45%	6s	3.31%	7s	4.20%	8s

Method	TSP100		ATSP100		OP100		PCTSP100		PDTSP100		ACVRPBTW	
	Gap	Time	Gap	Time	Gap	Time	Gap	Time	Gap	Time	Gap	Time
Oracle	0.00%	6m	0.00%	2m	0.00%	1.5m	0.00%	1.2h	0.00%	9.8m	0.00%	3.5h
GOAL-MTL	—	—	1.77%	1m	1.20%	38s	—	—	—	—	—	—
URS	0.57%	6s	2.26%	1.1m	0.45%	4s	1.06%	5s	4.98%	4s	9.95%	2.2m
SPACE	0.64%	5s	2.89%	1.4m	0.44%	5s	0.88%	5s	4.71%	5s	-0.52%	2.1m

Table 3: Zero-shot generalization on 24 unseen VRPs.

Method	Symmetric Gap (Time)	Asymmetric Gap (Time)	Average Gap	Symmetric Gap (Time)	Asymmetric Gap (Time)	Average Gap	Symmetric Gap (Time)	Asymmetric Gap (Time)	Average Gap
Problem	CVRPBLTW			OCVRPLTW			CVRPBLTW		
Oracle	0.00% (6.6m)	0.00% (6.6m)	0.00%	0.00% (3.5h)	0.00% (3.5h)	0.00%	0.00% (3.5h)	0.00% (3.5h)	0.00%
MVMoE	16.66% (16s)	—	—	3.90% (15s)	—	—	7.33% (16s)	—	—
MTPOMO	17.15% (10s)	—	—	4.37% (8s)	—	—	7.75% (8s)	—	—
ReLD-MTL	15.95% (12s)	—	—	3.16% (9s)	—	—	6.94% (9s)	—	—
URS	18.33% (10s)	13.82% (2.8m)	16.08%	5.12% (9s)	16.35% (2.8m)	10.74%	9.18% (8s)	10.18% (2.4m)	9.68%
SPACE	17.54% (11s)	4.16% (2.9m)	10.85%	4.26% (9s)	6.99% (2.6m)	5.63%	8.29% (8s)	-0.37% (2.3m)	3.96%
Problem	OCVRPBTW			OCVRPBTW			MDOCVRPLTW		
Oracle	0.00% (3.5h)	0.00% (6.6m)	0.00%	0.00% (6.6m)	0.00% (6.6m)	0.00%	0.00% (6.6m)	0.00% (6.6m)	0.00%
MVMoE	9.95% (15s)	—	—	9.42% (15s)	—	—	35.82% (2.1m)	—	—
MTPOMO	10.45% (6s)	—	—	9.94% (9s)	—	—	30.08% (1.5m)	—	—
ReLD-MTL	9.29% (8s)	—	—	8.43% (11s)	—	—	24.65% (1.8m)	—	—
URS	13.77% (7s)	14.45% (2.3m)	14.11%	10.05% (8s)	17.45% (2.5m)	13.75%	21.88% (1.1m)	24.30% (20m)	23.09%
SPACE	11.60% (7s)	5.48% (2.2m)	8.54%	9.62% (9s)	9.65% (2.7m)	9.64%	18.16% (1.1m)	15.35% (20m)	16.75%
Problem	CVRPLTW			OCVRPB			MDOCVRPLTW		
Oracle	0.00% (3.5h)	0.00% (3.5h)	0.00%	0.00% (3.5h)	0.00% (3.5h)	0.00%	0.00% (6.6m)	0.00% (6.6m)	0.00%
MVMoE	1.47% (16s)	—	—	7.09% (12s)	—	—	41.51% (2.1m)	—	—
MTPOMO	1.92% (9s)	—	—	7.34% (5s)	—	—	34.21% (1.5m)	—	—
ReLD-MTL	1.17% (11s)	—	—	5.36% (6s)	—	—	26.44% (1.8m)	—	—
URS	2.67% (9s)	12.22% (2.7m)	7.45%	9.35% (6s)	18.05% (2.5m)	13.70%	32.92% (1.3m)	15.26% (22m)	24.09%
SPACE	1.82% (9s)	2.26% (2.6m)	2.04%	7.33% (6s)	-1.34% (1.7m)	2.99%	27.29% (1.3m)	4.64% (21m)	15.97%
Problem	MDOCVRPTW			CVRPBTW			MDOCVRPB		
Oracle	0.00% (6.6m)	0.00% (6.6m)	0.00%	0.00% (6.6m)	0.00% (6.6m)	0.00%	0.00% (6.6m)	0.00% (6.6m)	0.00%
MVMoE	40.61% (2.1m)	—	—	16.86% (15s)	—	—	29.77% (1.5m)	—	—
MTPOMO	33.05% (1.5m)	—	—	17.22% (9s)	—	—	24.80% (1.1m)	—	—
ReLD-MTL	25.48% (1.8m)	—	—	16.09% (11s)	—	—	17.66% (1.2m)	—	—
URS	31.51% (1.3m)	15.38% (21m)	23.45%	18.15% (9s)	14.52% (2.6m)	16.33%	13.46% (47s)	25.95% (16m)	19.70%
SPACE	25.97% (1.2m)	4.73% (19m)	15.35%	17.57% (10s)	4.73% (2.7m)	11.15%	13.07% (47s)	11.03% (12m)	12.05%

Metrics & Inference We report the optimality gap (Gap) and inference time (Time) for each method. The optimality gap quantifies the discrepancy between the solutions generated by neural solvers and those obtained by oracle solvers. Note that we report the average gap for symmetric and asymmetric scenarios. For most NCO baselines, we execute the source code provided by the authors using default settings. Consistent with [14], we report the best result with $\times 8$ and $\times 128$ instance augmentation for symmetric and asymmetric instances, respectively. The mark (—) indicates that the method does not support the corresponding setting.

4.2 Performance Evaluation

Performance on Seen VRPs As shown in Table 2, SPACE remains highly competitive across the 12 seen variants among all comparable solvers and achieves smaller optimality gaps than URS on most tasks. Following the URS philosophy, we reduce reliance on problem-specific constraint states and use a model-agnostic masking function that handles diverse constraints during decoding (see Appendix H.4). While this design choice may yield inferior results on small-scale seen VRPs

Table 4: Scalability comparison between different solvers on complex VRP variants with 1000 nodes.

Method	Symmetric Gap (Time)	Asymmetric Gap (Time)	Average Gap	Symmetric Gap (Time)	Asymmetric Gap (Time)	Average Gap	Symmetric Gap (Time)	Asymmetric Gap (Time)	Average Gap
Problem	CVRPB1000			OCVRP1000			CVRPTW1000		
Oracle	0.00% (20m)	0.00% (20m)	0.00%	0.00% (20m)	0.00% (20m)	0.00%	0.00% (20m)	0.00% (20m)	0.00%
MTPOMO	25.77% (1.3m)	—	—	63.98% (1.3m)	—	—	37.57% (1.7m)	—	—
MVMoE	170.03% (1.0m)	—	—	149.38% (1.2m)	—	—	46.55% (1.7m)	—	—
ReLD-MTL	5.48% (1.0m)	—	—	24.75% (1.2m)	—	—	15.04% (1.6m)	—	—
URS	-4.54% (40s)	4.37% (37s)	-0.09%	14.84% (45s)	27.51% (51s)	21.18%	8.30% (1.3m)	4.20% (1.1m)	6.25%
SPACE	-4.16% (40s)	-19.10% (33s)	-11.63%	13.56% (44s)	10.28% (38s)	11.92%	7.34% (1.3m)	-2.92% (1.2m)	2.21%

compared to neural solvers that explicitly embed these states (e.g., ReLD-MTL), SPACE demonstrates a clear advantage on both unseen asymmetric variants (Table 3) and large-scale instances (Table 4).

Generalization on Unseen VRPs We evaluate the zero-shot generalization of SPACE across 98 unseen VRP variants. As shown in Table 3 (see Appendix I for detailed results), SPACE delivers the lowest average gap on most variants. Crucially, it achieves superior results on asymmetric variants while remaining competitive on symmetric ones, demonstrating its strong zero-shot generalization on both symmetric and asymmetric settings.

Results on Benchmark Dataset We evaluate SPACE on large-scale benchmark instances from CVRPLIB Set-X [32] and Set-XXL [33]. Note that all models are trained on 100-scale instances. As summarized in Table 5, SPACE still maintains its position as the best overall solver among all comparable neural solvers. These results further underscore the practical applicability of SPACE in real-world large-scale scenarios.

Table 5: Comparison on CVRPLIB Set-X and Set-XXL.

Method	500 < n ≤ 1K	1K < n ≤ 5K	5K < n ≤ 7K	ALL	Solved #
MTPOMO	16.80%	77.52%	OOM	—	32/34
MVMoE/4E	26.41%	234.60%	OOM	—	32/34
MVMoE/4E-L	19.61%	154.68%	OOM	—	32/34
RF-MVMoE	18.80%	108.79%	OOM	—	32/34
RF-TE	12.30%	36.23%	OOM	—	32/34
CaDA	334.84%	OOM	OOM	—	31/34
ReLD-MTL	9.44%	23.80%	OOM	—	32/34
URS	8.68%	14.69%	12.09%	9.20%	34/34
SPACE	7.86%	12.53%	11.76%	8.34%	34/34

Complete instance-level results are reported in Tables 15 and 16.

Scalability on Large-scale Realistic Problems To further assess scalability, we evaluate SPACE on symmetric and asymmetric VRP variants comprising 1,000 nodes. As shown in Table 4, SPACE consistently outperforms all evaluated baselines and achieves the best overall performance on all three evaluated variants. These results demonstrate the robust scalability of SPACE in addressing large-scale complex VRPs.

5 Ablation Study

We conduct ablation studies across 16 widely studied CVRP variants and their asymmetric counterparts to validate the contributions of BFR and WDAD. Table 6 reports the average gaps on symmetric and asymmetric variants. Replacing the entire BFR with a distance-based unified representation (similar to GOAL [13]) degrades the symmetric performance, while removing FPS results in significant degradation in both settings, indicating that stable pivot selection is necessary for using reference-distance features. The depot initialization and bidirectional coordinates (denoted as Bi.) also contribute to the final performance. For WDAD, replacing it with the original URS hypernetwork or reducing it to a single head both weaken performance, suggesting that decomposed multi-head updates are useful for transferring constraint logic across problem settings. Detailed per-variant results and the meaning of each ablation option are provided in Tables 19 to 21 in Appendix L, respectively.

Table 6: Ablation summary of SPACE.

Pivot	FPS	Depot	Bi.	WDAD	Avg-gap	
					Sym.	Asym.
×	×	×	×	3	7.67%	2.38%
5	✓	✓	✓	3	5.19%	2.04%
10	✓	✓	✓	3	5.50%	2.35%
20	✓	✓	✓	3	5.83%	1.54%
30	✓	✓	✓	3	5.70%	2.55%
8	×	✓	✓	3	83.10%	95.72%
8	✓	×	✓	3	5.85%	2.06%
8	✓	✓	×	3	5.80%	2.64%
8	✓	✓	✓	×	7.06%	3.82%
8	✓	✓	✓	1	5.58%	2.23%
8	✓	✓	✓	3	5.11%	1.27%

6 Conclusion, Limitation, and Future Work

In this work, we propose SPACE, a generalist neural routing framework for unifying symmetric and asymmetric VRPs. The core of SPACE is a bidirectional Fréchet representation that defines node positions in terms of incoming and outgoing distances to pivots selected via furthest pivot sampling, enabling a coordinate-free representation shared across distinct problem settings. Its generalization capability is further enhanced by weight-decomposed adaptive decoding, which separates geometry-invariant routing knowledge from constraint-specific decision logic. Extensive experiments on 110 VRP variants show that SPACE significantly improves performance in asymmetric settings while maintaining competitive performance on symmetric variants, and further scales to large benchmark instances without fine-tuning.

Limitation and Future Work A current limitation of SPACE is that it deliberately reduces reliance on problem-specific constraint states. We retain only essential decoder state signals and use a model-agnostic masking function to handle diverse constraints during decoding, which favors cross-problem transfer but can weaken constraint-aware performance on constraint-heavy variants. Improving the model’s constraint awareness while preserving model agnosticism is a key direction for future work.

References

- [1] Kubra Sar and Pezhman Ghadimi. A systematic literature review of the vehicle routing problem in reverse logistics operations. *Computers & Industrial Engineering*, 177:109011, 2023.
- [2] Keld Helsgaun. An extension of the lin-kernighan-helsgaun tsp solver for constrained traveling salesman and vehicle routing problems. *Roskilde: Roskilde University*, 12, 2017.
- [3] Thibaut Vidal. Hybrid genetic search for the cvrp: Open-source implementation and swap* neighborhood. *Computers & Operations Research*, 140:105643, 2022.
- [4] Yoshua Bengio, Andrea Lodi, and Antoine Prouvost. Machine learning for combinatorial optimization: a methodological tour d’horizon. *European Journal of Operational Research*, 290(2):405–421, 2021.
- [5] Yunpeng Ba, Xi Lin, Changliang Zhou, Ruihao Zheng, Zhenkun Wang, Xinyan Liang, Zhichao Lu, Jianyong Sun, Yuhua Qian, and Qingfu Zhang. Survey on neural routing solvers. *arXiv preprint arXiv:2602.21761*, 2026.
- [6] Chaitanya K Joshi, Thomas Laurent, and Xavier Bresson. An efficient graph convolutional network technique for the travelling salesman problem. *arXiv preprint arXiv:1906.01227*, 2019.
- [7] Yang Li, Jinpei Guo, Runzhong Wang, Hongyuan Zha, and Junchi Yan. Fast t2t: Optimization consistency speeds up diffusion-based training-to-testing solving for combinatorial optimization. *Advances in Neural Information Processing Systems*, 37:30179–30206, 2024.
- [8] Yeong-Dae Kwon, Jinho Choo, Byoungjip Kim, Iljoo Yoon, Youngjune Gwon, and Seungjai Min. Pomo: Policy optimization with multiple optima for reinforcement learning. *Advances in Neural Information Processing Systems*, 33:21188–21198, 2020.
- [9] Changliang Zhou, Xi Lin, Zhenkun Wang, Xialiang Tong, Mingxuan Yuan, and Qingfu Zhang. Instance-conditioned adaptation for large-scale generalization of neural routing solver. *IEEE Transactions on Intelligent Transportation Systems*, 2026.
- [10] Fei Liu, Xi Lin, Zhenkun Wang, Qingfu Zhang, Tong Xialiang, and Mingxuan Yuan. Multi-task learning for routing problem with cross-problem zero-shot generalization. In *Proceedings of the 30th ACM SIGKDD Conference on Knowledge Discovery and Data Mining*, pages 1898–1908, 2024.
- [11] Jianan Zhou, Zhiguang Cao, Yaoxin Wu, Wen Song, Yining Ma, Jie Zhang, and Chi Xu. Mvmoe: multi-task vehicle routing solver with mixture-of-experts. In *Proceedings of the 41st International Conference on Machine Learning*, pages 61804–61824, 2024.
- [12] Zhuoyi Lin, Yaoxin Wu, Bangjian Zhou, Zhiguang Cao, Wen Song, Yingqian Zhang, and Senthilnath Jayavelu. Cross-problem learning for solving vehicle routing problems. In *Proceedings of the Thirty-Third International Joint Conference on Artificial Intelligence*, pages 6958–6966, 2024.
- [13] Darko Drakulic, Sofia Michel, and Jean-Marc Andreoli. Goal: A generalist combinatorial optimization agent learner. In *The Thirteenth International Conference on Learning Representations*, 2025.

- [14] Changliang Zhou, Canhong Yu, Shunyu Yao, Xi Lin, Zhenkun Wang, Yu Zhou, and Qingfu Zhang. Urs: A unified neural routing solver for cross-problem zero-shot generalization. *arXiv preprint arXiv:2509.23413*, 2025.
- [15] Giulio Attenni, Viviana Arrigoni, Novella Bartolini, and Gaia Maselli. Drone-based delivery systems: A survey on route planning. *Ieee Access*, 11:123476–123504, 2023.
- [16] Jiwoo Son, Zhikai Zhao, Federico Berto, Chuanbo Hua, Changhyun Kwon, and Jinkyoo Park. Neural combinatorial optimization for real-world routing. *arXiv preprint arXiv:2503.16159*, 2025.
- [17] Jean Bourgain. On lipschitz embedding of finite metric spaces in hilbert space. *Israel Journal of Mathematics*, 52(1):46–52, 1985.
- [18] Wallace Alvin Wilson. On quasi-metric spaces. *American Journal of Mathematics*, 53(3):675–684, 1931.
- [19] Paolo Toth and Daniele Vigo. *The vehicle routing problem*. SIAM, 2002.
- [20] Fu Luo, Xi Lin, Fei Liu, Qingfu Zhang, and Zhenkun Wang. Neural combinatorial optimization with heavy decoder: Toward large scale generalization. In *Thirty-seventh Conference on Neural Information Processing Systems*, 2023.
- [21] Wouter Kool, Herke van Hoof, and Max Welling. Attention, learn to solve routing problems! In *International Conference on Learning Representations*, 2019.
- [22] Ziwei Huang, Jianan Zhou, Zhiguang Cao, and Yixin Xu. Rethinking light decoder-based solvers for vehicle routing problems. *International Conference on Learning Representations*, 2025.
- [23] Yeong-Dae Kwon, Jinho Choo, Iljoo Yoon, Minah Park, Duwon Park, and Youngjune Gwon. Matrix encoding networks for neural combinatorial optimization. *Advances in Neural Information Processing Systems*, 34:5138–5149, 2021.
- [24] Darko Drakulic, Sofia Michel, Florian Mai, Arnaud Sors, and Jean-Marc Andreoli. Bq-nco: Bisimulation quotienting for efficient neural combinatorial optimization. In *Thirty-seventh Conference on Neural Information Processing Systems*, 2023.
- [25] Ashish Vaswani, Noam Shazeer, Niki Parmar, Jakob Uszkoreit, Llion Jones, Aidan N Gomez, Łukasz Kaiser, and Illia Polosukhin. Attention is all you need. *Advances in Neural Information Processing Systems*, 30, 2017.
- [26] Jiri Matousek. *Lectures on discrete geometry*, volume 212. Springer Science & Business Media, 2013.
- [27] Shih-Yang Liu, Chien-Yi Wang, Hongxu Yin, Pavlo Molchanov, Yu-Chiang Frank Wang, Kwang-Ting Cheng, and Min-Hung Chen. Dora: Weight-decomposed low-rank adaptation. In *Forty-first International Conference on Machine Learning*, 2024.
- [28] Jingwen Li, Liang Xin, Zhiguang Cao, Andrew Lim, Wen Song, and Jie Zhang. Heterogeneous attentions for solving pickup and delivery problem via deep reinforcement learning. *IEEE Transactions on Intelligent Transportation Systems*, 23(3):2306–2315, 2021.
- [29] Ronald J Williams. Simple statistical gradient-following algorithms for connectionist reinforcement learning. *Machine Learning*, 8:229–256, 1992.
- [30] Federico Berto, Chuanbo Hua, Nayeli Gast Zepeda, André Hottung, Niels Wouda, Leon Lan, Junyoung Park, Kevin Tierney, and Jinkyoo Park. Routefinder: Towards foundation models for vehicle routing problems. *Transactions on Machine Learning Research*, 2025.
- [31] Han Li, Fei Liu, Zhi Zheng, Yu Zhang, and Zhenkun Wang. Cada: Cross-problem routing solver with constraint-aware dual-attention. In *Proceedings of the 42nd International Conference on Machine Learning*, 2025.
- [32] Eduardo Uchoa, Diego Pecin, Artur Pessoa, Marcus Poggi, Thibaut Vidal, and Anand Subramanian. New benchmark instances for the capacitated vehicle routing problem. *European Journal of Operational Research*, 257(3):845–858, 2017.
- [33] Florian Arnold, Michel Gendreau, and Kenneth Sörensen. Efficiently solving very large-scale routing problems. *Computers & operations research*, 107:32–42, 2019.
- [34] Oriol Vinyals, Meire Fortunato, and Navdeep Jaitly. Pointer networks. *Advances in Neural Information Processing Systems*, 28, 2015.

- [35] Irwan Bello, Hieu Pham, Quoc V Le, Mohammad Norouzi, and Samy Bengio. Neural combinatorial optimization with reinforcement learning. *arXiv preprint arXiv:1611.09940*, 2016.
- [36] Mohammadreza Nazari, Afshin Oroojlooy, Lawrence Snyder, and Martin Takác. Reinforcement learning for solving the vehicle routing problem. *Advances in Neural Information Processing Systems*, 31, 2018.
- [37] Liang Xin, Wen Song, Zhiguang Cao, and Jie Zhang. Step-wise deep learning models for solving routing problems. *IEEE Transactions on Industrial Informatics*, 17(7):4861–4871, 2020.
- [38] Minsu Kim, Junyoung Park, and Jinkyoo Park. Sym-nco: Leveraging symmetry for neural combinatorial optimization. *Advances in Neural Information Processing Systems*, 35:1936–1949, 2022.
- [39] Jianan Zhou, Yaixin Wu, Wen Song, Zhiguang Cao, and Jie Zhang. Towards omni-generalizable neural methods for vehicle routing problems. In *International Conference on Machine Learning*, 2023.
- [40] Han Fang, Zhihao Song, Paul Weng, and Yutong Ban. Invt: A generalizable routing problem solver with invariant nested view transformer. In *International Conference on Machine Learning*, 2024.
- [41] Changliang Zhou, Xi Lin, Zhenkun Wang, and Qingfu Zhang. Learning to reduce search space for generalizable neural routing solver. *arXiv preprint arXiv:2503.03137*, 2025.
- [42] Yuanyao Chen, Rongsheng Chen, Fu Luo, and Zhenkun Wang. Improving generalization of neural combinatorial optimization for vehicle routing problems via test-time projection learning. *Advances in Neural Information Processing Systems*, 2025.
- [43] Chengrui Gao, Haopu Shang, Ke Xue, Dong Li, and Chao Qian. Towards generalizable neural solvers for vehicle routing problems via ensemble with transferrable local policy. In *International Joint Conference on Artificial Intelligence*, 2024.
- [44] Fu Luo, Xi Lin, Yaixin Wu, Zhenkun Wang, Tong Xialiang, Mingxuan Yuan, and Qingfu Zhang. Boosting neural combinatorial optimization for large-scale vehicle routing problems. In *The Thirteenth International Conference on Learning Representations*, 2025.
- [45] Zhi Zheng, Changliang Zhou, Tong Xialiang, Mingxuan Yuan, and Zhenkun Wang. Udc: A unified neural divide-and-conquer framework for large-scale combinatorial optimization problems. In *Thirty-eighth Conference on Neural Information Processing Systems*, 2024.
- [46] Haoran Ye, Jiarui Wang, Helan Liang, Zhiguang Cao, Yong Li, and Fanzhang Li. Glop: Learning global partition and local construction for solving large-scale routing problems in real-time. In *Proceedings of the AAAI Conference on Artificial Intelligence*, volume 38, pages 20284–20292, 2024.
- [47] Zhang-Hua Fu, Kai-Bin Qiu, and Hongyuan Zha. Generalize a small pre-trained model to arbitrarily large tsp instances. In *Proceedings of the AAAI Conference on Artificial Intelligence*, volume 35, pages 7474–7482, 2021.
- [48] Ruizhong Qiu, Zhiqing Sun, and Yiming Yang. Dimes: A differentiable meta solver for combinatorial optimization problems. *Advances in Neural Information Processing Systems*, 35:25531–25546, 2022.
- [49] Yang Li, Jinpei Guo, Runzhong Wang, and Junchi Yan. T2t: From distribution learning in training to gradient search in testing for combinatorial optimization. In *Thirty-seventh Conference on Neural Information Processing Systems*, 2023.
- [50] Zhiqing Sun and Yiming Yang. Difusco: Graph-based diffusion solvers for combinatorial optimization. *Advances in Neural Information Processing Systems*, 36:3706–3731, 2023.
- [51] Jingwen Li, Yining Ma, Ruize Gao, Zhiguang Cao, Andrew Lim, Wen Song, and Jie Zhang. Deep reinforcement learning for solving the heterogeneous capacitated vehicle routing problem. *IEEE Transactions on Cybernetics*, 52(12):13572–13585, 2022.
- [52] Conghui Wang, Zhiguang Cao, Yaixin Wu, Long Teng, and Guohua Wu. Deep reinforcement learning for solving vehicle routing problems with backhauls. *IEEE Transactions on Neural Networks and Learning Systems*, 36(3):4779–4793, 2024.
- [53] Zhi Zheng, Shunyu Yao, Zhenkun Wang, Xialiang Tong, Mingxuan Yuan, and Ke Tang. Dpn: Decoupling partition and navigation for neural solvers of min-max vehicle routing problems. In *Proceedings of the 41st International Conference on Machine Learning*, pages 61559–61592, 2024.
- [54] Wenzheng Pan, Hao Xiong, Jiale Ma, Wentao Zhao, Yang Li, and Junchi Yan. Unico: On unified combinatorial optimization via problem reduction to matrix-encoded general tsp. In *The Thirteenth International Conference on Learning Representations*, 2025.

- [55] Yuepeng Zheng, Fu Luo, Zhenkun Wang, Yaoxin Wu, and Yu Zhou. Mtl-kd: Multi-task learning via knowledge distillation for generalizable neural vehicle routing solver. *Advances in Neural Information Processing Systems*, 2025.
- [56] Chenguang Wang, Zhang-Hua Fu, Pinyan Lu, and Tianshu Yu. Efficient training of multi-task neural solver for combinatorial optimization. *Transactions on Machine Learning Research*, 2025.
- [57] Jingwen Li, Liang Xin, Zhiguang Cao, Andrew Lim, Wen Song, and Jie Zhang. Heterogeneous attentions for solving pickup and delivery problem via deep reinforcement learning. *IEEE Transactions on Intelligent Transportation Systems*, 23(3):2306–2315, 2021.
- [58] Kaiming He, Xiangyu Zhang, Shaoqing Ren, and Jian Sun. Delving deep into rectifiers: Surpassing human-level performance on imagenet classification. In *Proceedings of the IEEE international conference on computer vision*, pages 1026–1034, 2015.
- [59] Niels A Wouda, Leon Lan, and Wouter Kool. Pyvrp: A high-performance vrp solver package. *INFORMS Journal on Computing*, 36(4):943–955, 2024.
- [60] Laurent Perron and Vincent Furnon. Or-tools, 2023. URL <https://developers.google.com/optimization/>.
- [61] Kaiming He, Xiangyu Zhang, Shaoqing Ren, and Jian Sun. Deep residual learning for image recognition. In *Proceedings of the IEEE Conference on Computer Vision and Pattern Recognition*, pages 770–778, 2016.
- [62] Dmitry Ulyanov, Andrea Vedaldi, and Victor Lempitsky. Instance normalization: The missing ingredient for fast stylization. *arXiv preprint arXiv:1607.08022*, 2016.
- [63] Yann LeCun, Léon Bottou, Genevieve B Orr, and Klaus-Robert Müller. Efficient backprop. In *Neural networks: Tricks of the trade*, pages 9–50. Springer, 2002.

A Related Work

A.1 Specialist Neural Solvers for Symmetric VRPs

Symmetric VRPs constitute the primary focus of neural routing research. Since the seminal application of Ptr-Nets to the TSP [34, 35], a succession of autoregressive constructive solvers has emerged for TSPs and CVRPs and already demonstrated promising results on small instances (e.g., 100-node TSPs) [36–38]. Notably, the Transformer-style Attention Model (AM) [21] and its multi-trajectory variant, POMO [8], have become the prevailing architectures. However, these models struggle with large-scale generalization, spurring researchers to improve them by varying-scale training [9, 39, 22], search space reduction [40–42], incorporating distance information [43, 9, 22], and alternative heavy decoder architectures [24, 20, 44]. Other paradigms mainly include problem decomposition [45, 46] and non-autoregressive heatmap generation augmented with additional searches (e.g., Monte Carlo tree search (MCTS) [47, 48] and 2-opt [49, 50]). Specialist solvers have also emerged for variants like heterogeneous fleets [51], pickup and delivery problems [28], CVRP with Backhauls [52], and min-max multiple VRPs [53]. Among these, constructive solvers are most common but are typically designed for VRPs and typically fail in asymmetric settings.

A.2 Specialist Neural Solvers for Asymmetric VRPs

Asymmetric VRPs (AVRPs) have garnered increasing attention due to their alignment with real-world logistics. Since AVRPs lack explicit coordinate information, research primarily focuses on node representations and on incorporating distance matrices. MatNet [23] reformulates ATSPs as a bipartite graph and introduces Mixed-Score Attention to incorporate distance information, establishing itself as the mainstream architecture. However, its reliance on fixed one-hot vectors hinders scalability. Pan et al. [54] address this limitation by introducing Pseudo One-hot Embeddings. ICAM [9] introduces k -nearest distance features and a lightweight distance-biased attention mechanism to enhance asymmetric spatial perception. Subsequently, Son et al. [16] further validate effectiveness on real-world scenarios by integrating neural adaptive bias and distance-based probabilistic sampling. Alternatively, the random identifier has been used for each node as its initial node feature in [24, 22], while GLOP [46] and UDC [45] leverage divide-and-conquer strategies to improve large-scale generalization. Despite these advancements, existing AVRP solvers generally employ highly specialized architectures to address the intrinsic asymmetry, which limits their applicability to symmetric problems and the development of a unified framework.

A.3 Generalist Neural Routing Solvers

To address the challenge of cross-problem generalization, growing attention has been directed toward multi-task learning capable of handling diverse routing problems. A primary approach formulates VRP variants as combinations of predefined constraints and trains a shared neural model [10, 11, 55, 31]. While achieving promising results with up to 48 variants [30], these methods are inherently bounded by manually specified constraint sets. More critically, they struggle to transfer to asymmetric settings. Another mainstream paradigm is adapter-based fine-tuning [56, 12]. Although GOAL [13] performs well in both seen symmetric and asymmetric VRPs, this paradigm lacks the capability for zero-shot generalization to unseen problems. Most recently, URS [14] replaces problem enumeration with a unified data representation and successfully covers over 100 (A)VRP variants without any fine-tuning. However, URS still relies on distinct positional representations for symmetric and asymmetric instances. In contrast, this work constructs a neural solver with zero-shot capabilities, enabling unified encoding and maintaining high performance across a wide range of VRPs.

B Setups of VRP Variants

B.1 Symmetry and Asymmetry

In symmetric VRP, the distance function is defined as a standard metric that satisfies non-negativity, identity, symmetry, and the triangle inequality. Under this formulation, the problem is naturally modeled as an undirected weighted graph embedded in a metric space, where the distance between any two nodes is reversible and directly determined by the underlying geometry. In contrast, asymmetric VRP relaxes the symmetry requirement (i.e., $d(v_i, v_j) \neq d(v_j, v_i)$), resulting in a fundamentally different distance structure. While non-negativity, identity of indiscernibles, and the triangle inequality are retained, the distance function strictly defines a quasimetric space. This change from a metric to a quasimetric formulation transforms the problem into a directed weighted graph with irreversible costs. Compared to the symmetric setting, it fundamentally modifies the structure of the solution space and the associated algorithmic properties.

Symmetry To construct symmetric instances, we randomly sample node coordinates from a 2D unit square, denoted as $\mathcal{X}_i \sim \mathcal{U}[0, 1]^2$. We then compute the distance $d(v_i, v_j)$ between nodes i and j , which is generally the Euclidean distance. The symmetric instance naturally forms a metric space (i.e., $d(v_i, v_j) = d(v_j, v_i), \forall v_i, v_j \in \mathcal{V}$).

Asymmetry To generate asymmetric VRP instances, we adopt the construction method in Kwon et al. [23], which directly generates distance matrices of problem instances. We initialize an integer-based directed distance matrix \mathbf{D} , where we independently sample $d(v_i, v_j)^{(0)}$ ($i \neq j$) from the discrete interval $[0, 10^6)$ and set the diagonal elements $d(v_i, v_i) = 0$. Due to the initial distance matrix typically violating the triangle inequality, we iteratively apply the min-plus closure rule: $d(v_i, v_j)^{(m+1)} = \min_l (d(v_i, v_l)^{(m)} + d(v_l, v_j)^{(m)})$ to enforce the quasimetric property. We compute this transitive closure in a min-plus semiring, terminating the process upon convergence. The resulting matrix \mathbf{D} strictly satisfies the triangle inequality $d(v_i, v_j) \leq d(v_i, v_k) + d(v_k, v_j)$ while generally maintaining asymmetry ($d(v_i, v_j) \neq d(v_j, v_i)$), thus forming an asymmetric metric VRP instance. Finally, we scale the costs as $\tilde{d}(v_i, v_j) = d(v_i, v_j)/\text{scaler}$ to ensure numerical stability for neural network training. Overall, the resulting asymmetric VRP instances are defined over a geometric space that is fundamentally different from the Euclidean metric space underlying symmetric VRP. While both settings satisfy the triangle inequality, the asymmetric distance structure induces a directed geometric space in which spatial relationships are inherently orientation-dependent, leading to a distinct notion of proximity and path optimality compared to the symmetric case.

B.2 Diverse Constraints

Capacity (C) For all PD-related variants except for PDTSP, we follow the configuration established by Zhou et al. [14] and set $C = 20$. For other VRP variants, we adopt the conventional settings in Kool et al. [21], Kwon et al. [8], where $C = 50$. Node demands are sampled from a discrete uniform distribution over the set $\{1, \dots, 9\}$.

Open Route (O) Under the Open Route configuration, vehicles are not mandated to return to the depot; thus, the final return leg is omitted from the total cost calculation. This relaxation propagates to other constraints: (i) for O-TW, the constraint $t_i \leq T_{\text{end}}$ is relaxed for the final destination, where T_{end} denotes the depot end time; (ii) for O-L, the route length limit is evaluated without considering the distance back to the depot.

Backhaul (B) Conventional CVRP limits operations to deliveries from a depot to linehaul nodes. The inclusion of backhaul constraints introduces backhaul nodes, requiring goods collection and return transport to the depot. Following the setting in Liu et al. [10], node demands are sampled from a discrete uniform distribution $U\{1, 2, \dots, 9\}$. We negate the demands of a randomly selected 20% subset, thereby designating nodes with positive and negative values as linehaul and backhaul customers, respectively. Notably, no precedence constraints are imposed between these two node categories. Following Zhou et al. [11], we mandate that the first customer in each route be a linehaul node to ensure solution feasibility, unless the remaining unvisited nodes consist entirely of backhauls.

Backhaul and Priority (BP) Building upon the B constraint, the BP variant incorporates additional precedence constraints regarding the service order: within each route, all linehaul nodes must be visited prior to any backhaul nodes. If a backhaul node is selected as the initial customer, the vehicle capacity is initialized to zero to reflect the absence of delivery load.

Duration Limit (L) For symmetric instances, node coordinates are sampled from $\mathcal{U}[0, 1]^2$, resulting in a maximum depot-to-customer distance of $\sqrt{2}$. The round-trip distance for a single-node route is thus capped at $2\sqrt{2} \approx 2.82$. To ensure feasibility across all instances, we set the duration limit to $L = 3.0$, consistent with the setting in Zhou et al. [11]. For asymmetric instances, we adopt the setting from Zhou et al. [14] and fix the duration limit at $L = 0.6$.

Time Windows (TW) For symmetric instances, the depot time window $[e_0, l_0]$ is defined as $[0, 3]$ with service time $s_0 = 0$. For customer nodes, we adopt the generation scheme from Zhou et al. [11] for time windows and set the service time s_i to 0.2. For asymmetric instances, we follow the [14] configuration by setting $[e_0, l_0] = [0, 1]$, while maintaining all other parameters consistent with the symmetric case.

Multi-Depot (MD) Consistent with Zhou et al. [14], we fix the depot count at 3, sampling coordinates from $\mathcal{U}[0, 1]^2$ identically to customer nodes. Unlike relaxed formulations that permit open routing, we enforce a strict *Return-to-Origin* constraint: every valid route must form a closed loop originating from and terminating at the same depot v_d . To unify multi-depot management within a single solution sequence, we model the transition between differing depots (e.g., $v_d \rightarrow v_e$) as a zero-cost virtual switch. This formulation allows the agent to sequentially optimize disjoint fleets while strictly excluding inter-depot travel distances from the objective function. For a detailed description of the selection strategy for multiple depots, please refer to Appendix B.3.

Prize Collecting (PC) Under the PC constraint setting, each customer node is associated with a prize and a penalty. While visiting a node accrues its prize, skipping it incurs a corresponding penalty. The objective is to minimize the total cost, defined as the sum of the solution length and the penalties for all unvisited nodes, subject to a minimum prize-collection requirement. Following the configuration in Kool et al. [21], the prizes are sampled from a continuous uniform distribution $\mathcal{U}(0, 4/n)$. The penalties are drawn from $\mathcal{U}(0, 3k_n/n)$, where $n = 100$ and $k_n = 4$. These parameters are scaled relative to the problem size to maintain consistent task difficulty.

Pickup and Delivery (PD) In the PD setting, nodes are partitioned into pickup and delivery pairs. Two fundamental requirements must be satisfied: (1) Precedence: each delivery node must be visited only after its corresponding pickup node; and (2) Completion: the vehicle is prohibited from returning to the depot until all collected loads have been delivered, ensuring that the vehicle is empty at the end of each route. Following the generation scheme in Li et al. [57], we designate node 0 as the depot for an instance of size n . We define nodes 1 to $n/2$ as pickup nodes and nodes $n/2 + 1$ to n as their corresponding delivery nodes. Specifically, for each pickup node i , we assign node $i + n/2$ as its unique delivery partner. For PDCVRP and its variants, we sample the demand for each pickup node from a discrete uniform distribution $\mathcal{U}\{1, 9\}$, while setting the demand of the paired delivery node to its negative equivalent to ensure load balance.

B.3 The Selection Strategy of Multiple Depots

Unlike prior works that treat depot returns implicitly [30], we explicitly parse the autoregressive action sequence into depot-rooted route segments. Let $\mathcal{V}_{\text{depot}} \subset \mathcal{V}$ denote the depot set. A nonempty route segment that starts from depot $v_d \in \mathcal{V}_{\text{depot}}$ must terminate at the same depot, i.e., it has the form $v_d \rightarrow v_{i_1} \rightarrow \dots \rightarrow v_{i_s} \rightarrow v_d$. Consecutive depot actions, such as $v_d \rightarrow v_e$, are interpreted only as a fleet-selection switch between two route segments. They are not physical travel arcs and do not modify the original distance function d .

Return-to-Origin Masking During decoding, we maintain an origin-depot state for each partial trajectory. When the current node is a customer, the masking function allows at most the origin depot among all depot nodes and assigns $-\infty$ logits to the other depots. This prevents invalid segments such as $v_d \rightarrow v_i \rightarrow v_e$ with $v_e \neq v_d$. For pickup-delivery variants, returning to the origin depot is further

masked until all picked-up loads in the current segment have been delivered. When the current node is already a depot and unserved customers remain, the decoder may either start a customer-serving segment from the current depot or select another depot as a control action that switches the active fleet. Once all customers have been served, only the current depot remains available, which terminates the trajectory.

The multi-depot objective is computed from the original distance matrix after the sequence has been generated. For a closed route segment $v_d \rightarrow v_{i_1} \rightarrow \dots \rightarrow v_{i_s} \rightarrow v_d$, its cost is

$$d(v_d, v_{i_1}) + \sum_{r=1}^{s-1} d(v_{i_r}, v_{i_{r+1}}) + d(v_{i_s}, v_d). \quad (7)$$

For open-route variants, the final return term is omitted. Consecutive depot-to-depot control actions contribute zero switch cost, but this zero cost is applied only at the sequence-evaluation level; the quasimetric distance matrix itself remains unchanged.

Global Lookahead Decoding A depot state is a branching point because the next useful route may start from any depot. Greedily decoding only from the currently active depot can therefore underuse distant fleets. To address this, when a trajectory is at a depot we evaluate every candidate depot $v_e \in \mathcal{V}_{\text{depot}}$ before committing to the next action. For each v_e , we query the decoder with the encoded representation of v_e and the outgoing distance vector from v_e to all nodes, while masking all depot nodes so that the comparison is based on feasible customer choices. We then record the highest customer-selection probability under this hypothetical start. If the best candidate depot is the current depot, the decoder directly selects the corresponding customer; otherwise, it first selects the best candidate depot as a fleet-switch action. For trajectories that are not at a depot, the standard autoregressive decoder is used without this lookahead.

C Detailed Theoretical Proofs

This section formalizes the geometric claims used in Section 2. We model VRP distances as finite quasimetrics, analyze stability under the symmetrized metric, and prove the key guarantees of Bidirectional Fréchet Representation: non-expansiveness, conditional non-contraction, coverage-induced separation, and the necessity of bidirectional coordinates.

C.1 Distance Quasimetrics in VRPs

Definition C.1 (Quasimetric Space). The node set of a routing problem is defined as a pair (\mathcal{V}, d) , where \mathcal{V} is a finite set and $d : \mathcal{V} \times \mathcal{V} \rightarrow \mathbb{R}_{\geq 0}$ satisfies:

1. $d(v_i, v_j) \geq 0$ (Non-negativity)
2. $d(v_i, v_i) = 0$ (Identity of indiscernibles; we assume $d(v_i, v_j) > 0$ if $i \neq j$)
3. $d(v_i, v_k) \leq d(v_i, v_j) + d(v_j, v_k)$ (Triangle Inequality)

Unlike a standard metric, a quasimetric does not require symmetry, i.e., $d(v_i, v_j) \neq d(v_j, v_i)$ is permissible [18].

Definition C.2 (Symmetrized Metric for Stability Analysis). Given a quasimetric space (\mathcal{V}, d) , we define the symmetrized metric $D_{\text{sym}} : \mathcal{V} \times \mathcal{V} \rightarrow \mathbb{R}_{\geq 0}$ as:

$$D_{\text{sym}}(v_i, v_j) = \max(d(v_i, v_j), d(v_j, v_i)). \quad (8)$$

This is a valid metric: non-negativity, symmetry, and identity follow directly from the quasimetric assumptions, and the triangle inequality follows since

$$\begin{aligned} D_{\text{sym}}(x, z) &= \max\{d(x, z), d(z, x)\} \\ &\leq \max\{d(x, y) + d(y, z), d(z, y) + d(y, x)\} \\ &\leq D_{\text{sym}}(x, y) + D_{\text{sym}}(y, z). \end{aligned} \quad (9)$$

This metric represents the "worst-case" separation between two nodes and serves as the upper bound for Lipschitz continuity analysis in Section 3.

Remark C.3 (On Symmetrization). While Bourgain's Theorem is originally stated for metric spaces (symmetric), theoretical guarantees for asymmetric spaces can be derived by considering the symmetrized metric $D_{\text{sym}}(v_i, v_j) = \max(d(v_i, v_j), d(v_j, v_i))$ or $D_{\text{sym}}(v_i, v_j) = d(v_i, v_j) + d(v_j, v_i)$. In our method, we explicitly handle asymmetry by constructing a *directed* embedding that concatenates representations for both $d(v_i, \cdot)$ and $d(\cdot, v_i)$.

C.2 Preservation of Geometric Logic via Bi-Lipschitz Embeddings

Here we formally show why minimizing distortion with respect to a symmetric reference metric is useful for preserving routing geometry. In the BFR analysis below, this reference metric is D_{sym} rather than the raw asymmetric quasimetric d .

Proposition C.4 (Constraint Preservation). *Let D be a metric on \mathcal{V} and let $\Phi : \mathcal{V} \rightarrow \ell_p$ be a bi-Lipschitz embedding with constants $\alpha, \beta > 0$ and distortion $\mathcal{D} = \beta/\alpha$. Then relative metric neighborhoods are preserved up to factor \mathcal{D} : for any distinct $v_i, v_j, v_k \in \mathcal{V}$ with $D(v_i, v_k) > 0$,*

$$\frac{\|\Phi(v_i) - \Phi(v_j)\|_p}{\|\Phi(v_i) - \Phi(v_k)\|_p} \leq \mathcal{D} \frac{D(v_i, v_j)}{D(v_i, v_k)}. \quad (10)$$

Moreover, any two-hop metric path obeys

$$\|\Phi(v_i) - \Phi(v_k)\|_p \leq \beta(D(v_i, v_j) + D(v_j, v_k)). \quad (11)$$

Proof. By the definition of a bi-Lipschitz embedding,

$$\alpha D(u, w) \leq \|\Phi(u) - \Phi(w)\|_p \leq \beta D(u, w) \quad \text{for all } u, w \in \mathcal{V}. \quad (12)$$

Using the upper bound for (v_i, v_j) and the lower bound for (v_i, v_k) gives

$$\frac{\|\Phi(v_i) - \Phi(v_j)\|_p}{\|\Phi(v_i) - \Phi(v_k)\|_p} \leq \frac{\beta D(v_i, v_j)}{\alpha D(v_i, v_k)} = \mathcal{D} \frac{D(v_i, v_j)}{D(v_i, v_k)}. \quad (13)$$

The two-hop bound follows from the upper bi-Lipschitz inequality and the triangle inequality of D :

$$\|\Phi(v_i) - \Phi(v_k)\|_p \leq \beta D(v_i, v_k) \leq \beta(D(v_i, v_j) + D(v_j, v_k)). \quad (14)$$

□

C.3 Bourgain's Embedding Theorem

We use Bourgain's theorem as a known external result. The theorem justifies the general principle that distances to reference subsets can encode finite metric geometry with controlled distortion.

Theorem C.5 ([17]). *Let (\mathcal{V}, d) be any finite metric space with $|\mathcal{V}| = n$. There exists an embedding $\Phi : \mathcal{V} \rightarrow \ell_2^k$ with dimension $k = O(\log^2 n)$ such that the distortion is bounded by $\mathcal{D}(\Phi) \leq C \log n$, where C is a universal constant independent of the metric space structure.*

After rescaling, the theorem ensures that for any pair of nodes $v_i, v_j \in \mathcal{V}$, the embedding Φ satisfies:

$$\frac{1}{C \log n} d(v_i, v_j) \leq \|\Phi(v_i) - \Phi(v_j)\|_2 \leq d(v_i, v_j). \quad (15)$$

The upper bound implies that the embedding is 1-Lipschitz, ensuring that distances in the vector space never exaggerate the true metric costs. The lower bound guarantees that the contraction of distances is logarithmically bounded, thereby preserving the distinguishability of distinct nodes and the integrity of local neighborhoods.

One standard construction behind the theorem samples reference subsets at logarithmically many scales. Let $J = \lfloor \log_2 n \rfloor$. For each scale $j \in \{1, \dots, J\}$ and repetition $t \in \{1, \dots, T\}$ with $T = \Theta(\log n)$, sample a subset $A_{j,t} \subseteq \mathcal{V}$ by including each point independently with probability 2^{-j} . For a nonempty subset A , define

$$\phi_A(v) = d(v, A) = \min_{a \in A} d(v, a), \quad (16)$$

and use the convention $\phi_\emptyset(v) = \text{diam}(\mathcal{V})$ for all v . Thus an empty sampled subset contributes only a constant coordinate and does not affect pairwise embedding distances. We then concatenate the subset-distance coordinates as

$$f(v_i) = \frac{1}{\sqrt{T \cdot J}} \bigoplus_{j=1}^J \bigoplus_{t=1}^T \phi_{A_{j,t}}(v_i). \quad (17)$$

For any fixed subset A under this convention, the map $v \mapsto \phi_A(v)$ is 1-Lipschitz:

$$|\phi_A(v_i) - \phi_A(v_j)| \leq d(v_i, v_j), \quad (18)$$

because the claim is trivial when $A = \emptyset$, and for $A \neq \emptyset$ the triangle inequality gives $d(v_i, A) \leq d(v_i, v_j) + d(v_j, A)$ and, by symmetry of the metric, the reverse inequality with v_i and v_j exchanged. Hence the normalized concatenation is non-expansive:

$$\|f(v_i) - f(v_j)\|_2^2 = \frac{1}{TJ} \sum_{j=1}^J \sum_{t=1}^T |\phi_{A_{j,t}}(v_i) - \phi_{A_{j,t}}(v_j)|^2 \leq d(v_i, v_j)^2. \quad (19)$$

The non-contraction lower bound in Eq. (15) is the nontrivial probabilistic separation part of Bourgain's theorem: with $T = \Theta(\log n)$ repetitions, the sampled subsets separate all pairs at the appropriate scale with high probability, yielding contraction at most $O(\log n)$ after a union bound over all node pairs. The deterministic BFR analyzed below has its own guarantee: unconditional non-expansiveness for arbitrary pivots and conditional non-contraction only under explicit pivot separation.

C.4 Bidirectional Fréchet Representation Construction

While Bourgain's Theorem guarantees the existence of a low-distortion embedding via random subsets, practical implementation requires a deterministic, computationally efficient construction. Here, we analyze the stability properties of the *Bidirectional Fréchet Representation* employed in our method. For arbitrary fixed-size pivot sets, the guarantee below is non-expansiveness; non-contraction requires a separate pivot-separation condition.

Definition C.6 (Bidirectional Fréchet Representation). Let (\mathcal{V}, d) be a finite quasimetric space and $\mathcal{P} = \{p_1, \dots, p_M\} \subset \mathcal{V}$ be a fixed set of M pivot nodes. We first define the unnormalized bidirectional pivot-coordinate vector

$$\tilde{\Phi}(v) = \bigoplus_{m=1}^M [d(v, p_m), d(p_m, v)]. \quad (20)$$

The Bidirectional Fréchet Representation used by SPACE is the normalized embedding

$$\Phi(v) = \frac{1}{\sqrt{2M}} \tilde{\Phi}(v). \quad (21)$$

Here \oplus denotes vector concatenation. The embedding space is equipped with the standard Euclidean norm $\|\cdot\|_2$.

We now prove that this specific construction satisfies a Lipschitz condition with respect to the symmetrized quasimetric geometry. This property shows that BFR does not artificially expand symmetrized geometric distances; feasibility constraints are still enforced by the decoder mask rather than by the embedding alone.

Proposition C.7 (1-Lipschitz Continuity in Quasimetric Spaces). *The normalized Bidirectional Fréchet Embedding $\Phi(v) = \frac{1}{\sqrt{2M}} \bigoplus_m [d(v, p_m), d(p_m, v)]$ is 1-Lipschitz (non-expansive) with respect to the symmetrized distance metric $D_{\text{sym}}(v_i, v_j) = \max(d(v_i, v_j), d(v_j, v_i))$. That is, for all $v_i, v_j \in \mathcal{V}$:*

$$\|\Phi(v_i) - \Phi(v_j)\|_2 \leq D_{\text{sym}}(v_i, v_j). \quad (22)$$

Proof. Consider the contribution of a single pivot p_m to the squared Euclidean distance in the embedding space. The component-wise difference vector for the m -th pivot is:

$$\delta_m = [d(v_i, p_m) - d(v_j, p_m), d(p_m, v_i) - d(p_m, v_j)]. \quad (23)$$

We analyze the two components separately using the triangle inequality inherent to the quasimetric d :

1. Outgoing Component: By the triangle inequality, $d(v_i, p_m) \leq d(v_i, v_j) + d(v_j, p_m)$. Rearranging gives $d(v_i, p_m) - d(v_j, p_m) \leq d(v_i, v_j)$. Similarly, $d(v_j, p_m) \leq d(v_j, v_i) + d(v_i, p_m)$ implies $d(v_j, p_m) - d(v_i, p_m) \leq d(v_j, v_i)$. Combining these, we bound the absolute difference:

$$|d(v_i, p_m) - d(v_j, p_m)| \leq \max(d(v_i, v_j), d(v_j, v_i)) = D_{\text{sym}}(v_i, v_j). \quad (24)$$

2. Incoming Component: By the triangle inequality, $d(p_m, v_i) \leq d(p_m, v_j) + d(v_j, v_i)$. Rearranging gives $d(p_m, v_i) - d(p_m, v_j) \leq d(v_j, v_i)$. Similarly, $d(p_m, v_j) \leq d(p_m, v_i) + d(v_i, v_j)$ implies $d(p_m, v_j) - d(p_m, v_i) \leq d(v_i, v_j)$. Thus, the absolute difference is also bounded:

$$|d(p_m, v_i) - d(p_m, v_j)| \leq \max(d(v_j, v_i), d(v_i, v_j)) = D_{\text{sym}}(v_i, v_j). \quad (25)$$

Now, summing over all M pivots and applying the normalization factor $\frac{1}{\sqrt{2M}}$:

$$\|\Phi(v_i) - \Phi(v_j)\|_2^2 = \sum_{m=1}^M \left(\frac{1}{2M} |d(v_i, p_m) - d(v_j, p_m)|^2 + \frac{1}{2M} |d(p_m, v_i) - d(p_m, v_j)|^2 \right) \quad (26)$$

$$\leq \frac{1}{2M} \sum_{m=1}^M (D_{\text{sym}}(v_i, v_j)^2 + D_{\text{sym}}(v_i, v_j)^2) \quad (27)$$

$$= \frac{1}{2M} \cdot 2M \cdot D_{\text{sym}}(v_i, v_j)^2 \quad (28)$$

$$= D_{\text{sym}}(v_i, v_j)^2. \quad (29)$$

Taking the square root completes the proof:

$$\|\Phi(v_i) - \Phi(v_j)\|_2 \leq D_{\text{sym}}(v_i, v_j). \quad (30)$$

□

Proposition C.8 (Conditional Non-Contraction under Pivot Separation). *For the normalized BFR in Proposition C.7, define the pivot separation score*

$$s_{\mathcal{P}}(v_i, v_j) = \max_{p \in \mathcal{P}} \max \{ |d(v_i, p) - d(v_j, p)|, |d(p, v_i) - d(p, v_j)| \}. \quad (31)$$

Then, for all $v_i, v_j \in \mathcal{V}$,

$$\frac{s_{\mathcal{P}}(v_i, v_j)}{\sqrt{2M}} \leq \|\Phi(v_i) - \Phi(v_j)\|_2 \leq D_{\text{sym}}(v_i, v_j). \quad (32)$$

Consequently, if the pivot set is η -separating with respect to D_{sym} , i.e.,

$$s_{\mathcal{P}}(v_i, v_j) \geq \eta D_{\text{sym}}(v_i, v_j) \quad \text{for all } v_i \neq v_j, \quad (33)$$

then BFR is bi-Lipschitz with respect to D_{sym} and has distortion at most $\sqrt{2M}/\eta$. Without this separation condition, an arbitrary pivot subset can collapse distinct nodes, so no bounded-distortion guarantee is claimed.

Proof. The upper bound is exactly Proposition C.7. For the lower bound, choose a pivot-coordinate pair attaining $s_{\mathcal{P}}(v_i, v_j)$. Since $\|\Phi(v_i) - \Phi(v_j)\|_2$ is the Euclidean norm of all normalized coordinate differences, it is at least the magnitude of this single normalized coordinate:

$$\|\Phi(v_i) - \Phi(v_j)\|_2 \geq \frac{s_{\mathcal{P}}(v_i, v_j)}{\sqrt{2M}}. \quad (34)$$

If $s_{\mathcal{P}}(v_i, v_j) \geq \eta D_{\text{sym}}(v_i, v_j)$ for every distinct pair, then

$$\frac{\eta}{\sqrt{2M}} D_{\text{sym}}(v_i, v_j) \leq \|\Phi(v_i) - \Phi(v_j)\|_2 \leq D_{\text{sym}}(v_i, v_j), \quad (35)$$

which is the bi-Lipschitz condition with $\alpha = \eta/\sqrt{2M}$ and $\beta = 1$. The distortion is therefore at most $\beta/\alpha = \sqrt{2M}/\eta$. \square

Proposition C.9 (Coverage-Induced Separation). *Let $\mathcal{P} \subseteq \mathcal{V}$ be a pivot set with $M = |\mathcal{P}|$ and covering radius*

$$\rho_{\text{sym}}(\mathcal{P}) = \max_{v \in \mathcal{V}} \min_{p \in \mathcal{P}} D_{\text{sym}}(v, p) \quad (36)$$

under the symmetrized metric D_{sym} . For any two nodes $v_i, v_j \in \mathcal{V}$, the pivot separation score in Proposition C.8 satisfies

$$s_{\mathcal{P}}(v_i, v_j) \geq (D_{\text{sym}}(v_i, v_j) - 2\rho_{\text{sym}}(\mathcal{P}))_+, \quad (37)$$

where $(a)_+ = \max(a, 0)$. Consequently, the normalized BFR satisfies

$$\|\Phi(v_i) - \Phi(v_j)\|_2 \geq \frac{(D_{\text{sym}}(v_i, v_j) - 2\rho_{\text{sym}}(\mathcal{P}))_+}{\sqrt{2M}}. \quad (38)$$

Proof. The claim is trivial when $D_{\text{sym}}(v_i, v_j) \leq 2\rho_{\text{sym}}(\mathcal{P})$, since $s_{\mathcal{P}}(v_i, v_j) \geq 0$. We therefore consider the case $D_{\text{sym}}(v_i, v_j) > 2\rho_{\text{sym}}(\mathcal{P})$.

By the definition of the covering radius, there exists a pivot $p \in \mathcal{P}$ such that $D_{\text{sym}}(v_j, p) \leq \rho_{\text{sym}}(\mathcal{P})$. Hence both $d(v_j, p) \leq \rho_{\text{sym}}(\mathcal{P})$ and $d(p, v_j) \leq \rho_{\text{sym}}(\mathcal{P})$.

If $D_{\text{sym}}(v_i, v_j) = d(v_i, v_j)$, then the quasimetric triangle inequality gives

$$d(v_i, v_j) \leq d(v_i, p) + d(p, v_j), \quad (39)$$

and therefore $d(v_i, p) \geq D_{\text{sym}}(v_i, v_j) - \rho_{\text{sym}}(\mathcal{P})$. Combining this with $d(v_j, p) \leq \rho_{\text{sym}}(\mathcal{P})$ yields

$$|d(v_i, p) - d(v_j, p)| \geq D_{\text{sym}}(v_i, v_j) - 2\rho_{\text{sym}}(\mathcal{P}). \quad (40)$$

If $D_{\text{sym}}(v_i, v_j) = d(v_j, v_i)$, then

$$d(v_j, v_i) \leq d(v_j, p) + d(p, v_i), \quad (41)$$

so $d(p, v_i) \geq D_{\text{sym}}(v_i, v_j) - \rho_{\text{sym}}(\mathcal{P})$. Since $d(p, v_j) \leq \rho_{\text{sym}}(\mathcal{P})$, we have

$$|d(p, v_i) - d(p, v_j)| \geq D_{\text{sym}}(v_i, v_j) - 2\rho_{\text{sym}}(\mathcal{P}). \quad (42)$$

In both cases, at least one outgoing or incoming pivot coordinate separates v_i and v_j by the stated amount, proving the lower bound on $s_{\mathcal{P}}(v_i, v_j)$. The lower bound on $\|\Phi(v_i) - \Phi(v_j)\|_2$ then follows directly from Proposition C.8. \square

Remark C.10 (Connection to Furthest Pivot Sampling). Proposition C.9 explains why reducing the pivot covering radius improves the non-contraction behavior of BFR: node pairs whose symmetrized distance is larger than $2\rho_{\text{sym}}(\mathcal{P})$ must be separated by at least one pivot-distance coordinate. In the implementation, FPS is performed with $d_{\text{fps}}(u, v) = \frac{1}{2}(d(u, v) + d(v, u))$ for smoother coverage. Since $d_{\text{fps}}(u, v) \leq D_{\text{sym}}(u, v) \leq 2d_{\text{fps}}(u, v)$, a small covering radius under d_{fps} also controls $\rho_{\text{sym}}(\mathcal{P})$ up to a constant factor, while the final BFR still retains the directed coordinates $d(v, p)$ and $d(p, v)$.

Remark C.11 (Handling Asymmetry via Symmetric Embeddings). A fundamental challenge in embedding asymmetric VRPs is that standard vector spaces (like ℓ_2) are symmetric norms. One might worry that mapping a directed graph to ℓ_2 loses information. However, Proposition C.7 only asserts *stability* (closeness preservation), not *isometry* or unconditional low distortion. The asymmetry is explicitly encoded in the *values* of the coordinates (i.e., $\Phi(v)$ contains both $d(v, p)$ and $d(p, v)$). Thus, the neural network can learn a non-symmetric decoding function $f(\Phi(v_i), \Phi(v_j)) \approx d(v_i, v_j)$ even though the metric $\|\Phi(v_i) - \Phi(v_j)\|_2$ is symmetric.

Corollary C.12 (Necessity of Bidirectionality for Directional Identifiability). *Let $\mathcal{P} = \{p_m\}_{m=1}^M \subset \mathcal{V}$ be a fixed pivot set. A normalized unidirectional embedding $\Phi_{\text{out}}(v) = \frac{1}{\sqrt{M}} \bigoplus_{m=1}^M [d(v, p_m)]$ can collapse nodes that are indistinguishable by their outgoing distances to \mathcal{P} but differ in their incoming geometry. More precisely, there exists a finite quasimetric space and distinct nodes v_i, v_j such that*

$$\Phi_{\text{out}}(v_i) = \Phi_{\text{out}}(v_j) \quad \text{while} \quad \Phi(v_i) \neq \Phi(v_j), \quad (43)$$

where $\Phi(v) = \frac{1}{\sqrt{2M}} \bigoplus_{m=1}^M [d(v, p_m), d(p_m, v)]$ is the normalized bidirectional Fréchet representation. Therefore, bidirectionality is necessary to retain directional information relative to the chosen pivots. This statement does not claim that Φ is globally injective for an arbitrary pivot subset; such a guarantee would require additional assumptions on \mathcal{P} .

Proof. It suffices to construct one asymmetric example. Let $\mathcal{V} = \{p, v_i, v_j\}$ and let d be the shortest-path distance induced by the directed graph with edge lengths

$$p \rightarrow v_i : 2, \quad p \rightarrow v_j : 1, \quad v_i \rightarrow p : 1, \quad v_j \rightarrow p : 1, \quad v_i \rightarrow v_j : 1, \quad v_j \rightarrow v_i : 2.$$

Shortest-path distances define a valid quasimetric, so the triangle inequality holds automatically. In particular,

$$d(v_i, p) = d(v_j, p) = 1, \quad d(p, v_i) = 2, \quad d(p, v_j) = 1.$$

Choose the pivot set $\mathcal{P} = \{p\}$. Then the outgoing-only representation collapses the two nodes:

$$\Phi_{\text{out}}(v_i) = [d(v_i, p)] = [1] \quad \text{and} \quad \Phi_{\text{out}}(v_j) = [d(v_j, p)] = [1]. \quad (44)$$

Hence $\Phi_{\text{out}}(v_i) = \Phi_{\text{out}}(v_j)$ even though $v_i \neq v_j$.

Bidirectionality: The normalized Bidirectional Fréchet Embedding $\Phi(v_i) = \frac{1}{\sqrt{2}} [d(v_i, p), d(p, v_i)]$ incorporates the ingress distances:

$$\Phi(v_i) = \frac{1}{\sqrt{2}} [d(v_i, p), d(p, v_i)] = \frac{1}{\sqrt{2}} [1, 2], \quad \Phi(v_j) = \frac{1}{\sqrt{2}} [d(v_j, p), d(p, v_j)] = \frac{1}{\sqrt{2}} [1, 1]. \quad (45)$$

Therefore $\Phi(v_i) \neq \Phi(v_j)$, and in fact

$$\|\Phi(v_i) - \Phi(v_j)\|_2 = \frac{1}{\sqrt{2}}. \quad (46)$$

This proves the strict informational advantage claimed here: a unidirectional Fréchet representation can lose directional distinctions that the bidirectional one preserves. What follows is the necessity of the extra coordinates for asymmetric identifiability relative to the chosen pivots, not a global injectivity guarantee for arbitrary pivot subsets. \square

D Implementation Details of Furthest Pivot Sampling

The representational power of the SPACE framework depends critically on the spatial distribution of the pivot set \mathcal{P} . While the main text outlines the theoretical motivation for Furthest Pivot Sampling (FPS), this appendix details the specific implementation strategies for metric symmetrization, training stochasticity, and inference-time augmentation.

D.1 Metric Symmetrization for Pivot Selection

In asymmetric VRPs, the raw distance matrix \mathbf{D} implies a directed graph topology where $d(v_i, v_j) \neq d(v_j, v_i)$. Standard FPS assumes a symmetric metric space to define a unique "distance" between nodes. To resolve this ambiguity without altering the underlying problem structure, we compute the pivot set \mathcal{P} based on a symmetrized reference metric d_{fps} . We define this metric as the mean of the bidirectional costs:

$$d_{\text{fps}}(v_i, v_j) = \frac{d(v_i, v_j) + d(v_j, v_i)}{2}. \quad (47)$$

Proposition D.1 (Metricity and Coverage of FPS). *If d is a quasimetric, then d_{fps} is a metric. Let $\mathcal{P}_{\text{init}} \subseteq \mathcal{V}$ be fixed, and let \mathcal{P}_M be the pivot set obtained by applying the greedy rule in Eq. (4) until $|\mathcal{P}_M| = M$. Define the covering radius*

$$R(\mathcal{P}) = \max_{v \in \mathcal{V}} \min_{p \in \mathcal{P}} d_{\text{fps}}(v, p). \quad (48)$$

If \mathcal{P}^ minimizes $R(\mathcal{P})$ among all M -point pivot sets that contain the same initial seeds $\mathcal{P}_{\text{init}}$, then*

$$R(\mathcal{P}_M) \leq 2R(\mathcal{P}^*). \quad (49)$$

Proof. Symmetry and identity of indiscernibles for d_{fps} follow directly from the definition and the corresponding quasimetric assumptions on d . For the triangle inequality, for any $x, y, z \in \mathcal{V}$,

$$d_{\text{fps}}(x, z) = \frac{d(x, z) + d(z, x)}{2} \quad (50)$$

$$\leq \frac{d(x, y) + d(y, z) + d(z, y) + d(y, x)}{2} \quad (51)$$

$$= d_{\text{fps}}(x, y) + d_{\text{fps}}(y, z). \quad (52)$$

Thus d_{fps} is a metric.

Let $r = R(\mathcal{P}_M)$ and $r^* = R(\mathcal{P}^*)$. Suppose, for contradiction, that $r > 2r^*$. Let x be a point whose distance to \mathcal{P}_M is r , and let $q_1, \dots, q_{M-|\mathcal{P}_{\text{init}}|}$ be the pivots added greedily after initialization. Because covering radii only decrease during furthest-first traversal, each q_a was at a distance of at least r from all previously selected pivots when it was chosen; also, x is at a distance of at least r from every pivot in \mathcal{P}_M . Hence the points $\{x, q_1, \dots, q_{M-|\mathcal{P}_{\text{init}}|}\}$ are pairwise more than $2r^*$ apart under d_{fps} .

Every point of this set must be within distance r^* of some center in \mathcal{P}^* . None can be covered by an initial seed, since each is more than r^* away from all seeds. Moreover, two of them cannot be covered by the same non-seed center in \mathcal{P}^* ; otherwise, the triangle inequality would put them within distance at most $2r^*$ of each other. This would require $M - |\mathcal{P}_{\text{init}}| + 1$ distinct non-seed centers in \mathcal{P}^* , but only $M - |\mathcal{P}_{\text{init}}|$ are available. This contradiction proves $r \leq 2r^*$. \square

Remark D.2. While the theoretical Lipschitz bound (Proposition C.7) utilizes the maximum distance D_{sym} to guarantee a strict upper bound, we employ the mean distance d_{fps} for pivot sampling. This is because the mean provides smoother density estimates of the underlying topology, thereby avoiding outlier effects caused by extreme one-way penalties often encountered in asymmetric VRPs. Using d_{fps} ensures that the selected pivots cover the topology uniformly, regardless of edge directionality. Crucially, this symmetrization applies *only* to the selection indices; the final embedding $\Phi(v)$ retains the asymmetric distance coordinates $d(v_i, p_m)$ and $d(p_m, v_i)$ up to the global normalization factor, preserving the directed topology required for routing.

D.2 Seed Initialization and Training Strategy

To prevent the model from overfitting to a fixed geometric constellation, we introduce stochasticity into the pivot generation process during training. We initialize the pivot set \mathcal{P}_{init} not just with the depot node, but with a stochastic combination of the depot and a randomly sampled customer node.

Formally, let \mathcal{V}_{depot} denote the set of depot nodes (typically $|\mathcal{V}_{depot}| = 1$ for standard CVRP and $|\mathcal{V}_{depot}| = 3$ for MDCVRP). For each training instance, we construct the initial pivot set \mathcal{P}_{init} as:

$$\mathcal{P}_{init} = \mathcal{V}_{depot} \cup \{v_{rand}\}, \quad \text{where } v_{rand} \sim \text{Uniform}(\mathcal{V} \setminus \mathcal{V}_{depot}). \quad (53)$$

The FPS algorithm then iteratively selects the remaining $M - |\mathcal{P}_{init}|$ pivots relative to this set. This strategy forces the encoder to learn robust representations that are invariant to the choice of reference points, effectively serving as a geometric regularization technique.

D.3 Pivot-Induced Multi-View Augmentation (Inference)

Standard test-time augmentation techniques, such as coordinate rotation or flipping, are not applicable to coordinate-free embeddings. Instead, we leverage the pivot-based architecture to generate diverse "views" of the same problem instance. By varying the pivot set \mathcal{P} , we alter the embedding $\Phi(v)$, thereby probing the solution space from different geometric perspectives.

We implement a deterministic yet diverse augmentation schedule based on the augmentation factor:

1. **Phase 1 (Customer Traversal):** For augmentations $\alpha \in \{1, \dots, \min(N_{aug}, |\mathcal{V}_{customer}|\}\}$, we systematically seed the FPS with the depot set and the α -th customer from a fixed random permutation of the customer set $\mathcal{V}_{customer}$. This ensures that for small N_{aug} , the model views the graph from maximally distinct vantage points.
2. **Phase 2 (Dual-Customer Seeding):** If $N_{aug} > |\mathcal{V}_{customer}|$, we exhaust single-customer seeds and transition to dual-customer seeding. We initialize \mathcal{P}_{init} with the depot set and two distinct customers selected at random. This increases the entropy of the initial geometric frame, generating further diverse embeddings for deep search.

Given the resulting batch of N_{aug} solutions, we select the final solution π^* that minimizes the objective function: $\pi^* = \arg \min_m \mathcal{J}(\pi_T)$.

D.4 Computational Overhead

We implement FPS using a vectorized approach to minimize computational overhead. Rather than recomputing pairwise distances at each step, we maintain a distance cache vector $\delta \in \mathbb{R}^{|\mathcal{V}|}$, where δ_i stores the minimum distance from node v_i to the current set of selected pivots.

Algorithm 1 summarizes the procedure. By efficiently utilizing the ‘scatter’ and ‘gather’ operations on the GPU, the computational cost of pivot selection becomes negligible compared to that of the Transformer encoder-decoder operations.

Algorithm 1 Vectorized Furthest Pivot Sampling with Seeds

Input: Symmetrized Distance Matrix D_{fps} , Number of pivots M , Initial pivot set $\mathcal{P}_{init} \subset \mathcal{V}$

Output: Pivot Indices \mathcal{P}

Initialize pivot list $\mathcal{P} \leftarrow \mathcal{P}_{init}$

Initialize distance cache $\delta \leftarrow \infty$

for each pivot $p \in \mathcal{P}_{init}$ **do**

Update cache: $\delta \leftarrow \min(\delta, D_{fps}[:, p])$

end for

while $|\mathcal{P}| < M$ **do**

Select next pivot: $p_{next} \leftarrow \arg \max(\delta)$

Add to list: $\mathcal{P} \leftarrow \mathcal{P} \cup \{p_{next}\}$

Update cache: $\delta \leftarrow \min(\delta, D_{fps}[:, p_{next}])$

Mask selected: $\delta[p_{next}] \leftarrow -\infty$

end while

E Implementation Details of Weight-Decomposed Adaptive Decoding

In this section, we elaborate on the implementation of the weight-decomposed adaptive decoding strategy described in Section 3.2. We employ a specialized variant of DoRA [27] designed for multi-attribute routing tasks, where constraint-specific logic is learned via additive weight updates conditioned on the multi-hot problem representation λ .

Task Attributes and Architecture The adaptation mechanism is conditioned on a binary task attribute vector $\lambda \in \{0, 1\}^{10}$, which encodes the presence of specific routing constraints. For each attention projection matrix in the decoder (query, key, value, and constraint embeddings), the final effective weight $W_{\text{eff}}^{(\lambda)}$ is computed as the sum of a shared base weight W_0 and a task-specific update ΔW :

$$W_{\text{eff}}^{(\lambda)} = W_0 + \Delta W^{(\lambda)}. \quad (54)$$

This ensures that W_0 captures universal geometric reasoning while $\Delta W^{(\lambda)}$ specializes in constraint logic.

Multi-Head DoRA Layer We implement a **TaskDoRALayer** that computes $\Delta W^{(\lambda)}$ by aggregating updates from active constraints. To enhance the representational capacity for complex constraints, each task attribute uses H independent heads, each a low-rank DoRA adapter.

For each attribute λ_j and each head $\eta \in \{1, \dots, H\}$, we maintain three learnable parameters:

- Directional matrices $W_{\text{down},\eta}^{(j)} \in \mathbb{R}^{r \times d_{\text{in}}}$ and $W_{\text{up},\eta}^{(j)} \in \mathbb{R}^{d_{\text{out}} \times r}$.
- A magnitude vector $g_\eta^{(j)} \in \mathbb{R}^{d_{\text{out}}}$.

The update contribution δ_j for attribute λ_j is the summation over its heads:

$$\delta_j = \sum_{\eta=1}^H g_\eta^{(j)} \odot \frac{W_{\text{up},\eta}^{(j)} W_{\text{down},\eta}^{(j)}}{\|W_{\text{up},\eta}^{(j)} W_{\text{down},\eta}^{(j)}\|_{\text{row}} + \epsilon}, \quad (55)$$

where \odot denotes row-wise broadcasting multiplication and $\|\cdot\|_{\text{row}}$ is the ℓ_2 norm along the input dimension of each output row.

The final task-specific update $\Delta W^{(\lambda)}$ is the mean aggregation of all active attribute updates:

$$\Delta W^{(\lambda)} = \frac{1}{Z(\lambda)} \sum_{j:\lambda_j=1} \delta_j, \quad Z(\lambda) = \max(1, \|\lambda\|_1). \quad (56)$$

Using the mean (rather than sum) prevents magnitude explosion when multiple constraints are active simultaneously, preserving the scale of the effective weights. The normalization by $Z(\lambda)$ averages active-attribute updates when constraints are present and yields $\Delta W^{(\lambda)} = 0$ when no attribute is active, so the decoder falls back to the shared base weight W_0 .

Initialization Strategy Proper initialization is critical for the additive formulation. We initialize parameters to ensure that the model starts with $\Delta W \approx \mathbf{0}$, effectively behaving as the base model initially:

- The down-projection tensor $W_{\text{down}}^{(j)}$ is initialized with Kaiming uniform initializer using $a = \sqrt{5}$ [58]. Under the fan-in convention for the stacked tensor $W_{\text{down}}^{(j)} \in \mathbb{R}^{H \times r \times d_{\text{in}}}$, this is equivalent to $\mathcal{U}(-1/\sqrt{rd_{\text{in}}}, 1/\sqrt{rd_{\text{in}}})$.
- $W_{\text{up},\eta}^{(j)} \sim \mathcal{N}(0, 0.01^2)$, matching the small random initialization used to avoid zero direction vectors.
- $g_\eta^{(j)} = \mathbf{0}$.

The initialization of $g_\eta^{(j)}$ to zero guarantees that the initial contribution of any constraint adapter is null, allowing the optimization trajectory to gradually introduce constraint-specific logic as needed.

F Multi-hot Problem Representation

Based on UDR, we design a 10-dimensional multi-hot problem representation $\lambda \in \{0, 1\}^{10}$ to characterize the underlying constraints of each problem. To ensure a concise yet comprehensive encoding, we integrate specific attributes into unified categories. Thus, compared to the URS [14], we make the following changes: (1) Since our spatial pivot-aligned representation exists for any problem, we do not use it for problem representation; (2) For time-related constraints (Earliest Arrival Time, Latest Arrival Time, and Service Time), we consolidate them into a single Time indicator; and (3) To ensure a compact problem representation, we unify delivery and linehaul nodes under a single delivery attribute, the distinction between backhaul and PD constraints is subsequently established through the co-occurrence of this attribute with either a backhaul or a pickup indicator.

Rather than capturing numerical values, this multi-hot vector λ serves as a high-level descriptor of the problem’s properties. By encoding whether an instance satisfies specific constraints, this representation enables the adaptive adjustment of model parameters based on the problem variant at hand.

F.1 Problem Representations of Seen VRPs

As illustrated in Table 7, we train SPACE across 12 diverse VRP variants to ensure that every feature within the UDR is activated at least once during the learning phase. Following Zhou et al. [14], the selection of the 12 training problems is guided by a "minimum redundancy" principle: we ensure that most attributes in UDR appear in at least two distinct problem types during training, which helps prevent the model from overfitting a specific attribute to a single problem type. The only two exceptions are the Penalty and Pickup attributes, as preliminary experiments have shown that exposure in a single problem type is sufficient for generalization to variants such as SPCTSP and PDCVRP.

F.2 Problem Representations of Unseen VRPs

We construct 98 unseen variants to further highlight the broad applicability of SPACE, each incorporating at least one of nine constraints to reflect diverse real-world scenarios. Detailed representations for all unseen symmetric and asymmetric VRP variants are provided in Table 8 and Table 9, respectively.

Oracle Solvers We use classical solvers to obtain the oracle solutions for computing optimality gaps. Specifically, the oracle solvers include HGS-PyVRP [59], LKH3 [2], and OR-Tools [60]. We run LKH3 [2] with 10000 trials and 1 run [21]. For HGS-PyVRP and OR-Tools, we run them on a single CPU core with a time limit of 20s [31]. The oracle solver used for each VRP variant is listed in the Oracle column of the following tables.

Table 7: Problem representations for 12 seen routing problems in our experiments.

Problem	Oracle	Demand	Prize	Penalty	Time	Depot	Pickup	Backhaul	Delivery	Sub-routes	Open Route
ATSP	LKH-3										
TSP	LKH-3										
CVRP	PyVRP	✓				✓			✓	✓	
ACVRP	PyVRP	✓				✓			✓	✓	
OP	Compass		✓			✓					
PCTSP	ILS		✓	✓		✓					
PDTSP	LKH-3					✓	✓		✓		
CVRPTW	PyVRP	✓			✓	✓	✓		✓	✓	
OCVRP	LKH-3	✓				✓			✓	✓	
CVRPB	OR-Tools	✓				✓		✓	✓	✓	✓
OCVRPTW	OR-Tools	✓			✓	✓			✓	✓	✓
ACVRPBTW	OR-Tools	✓			✓	✓		✓	✓	✓	

Table 8: Problem representations of 46 unseen symmetric VRP variants for zero-shot generalization.

Problem	Oracle	Demand	Prize	Penalty	Time	Depot	Pickup	Backhaul	Delivery	Sub-routes	Open Route
CVRPL	LKH-3	✓				✓			✓	✓	
OCVRPB	OR-Tools	✓				✓		✓	✓		✓
CVRPBL	OR-Tools	✓				✓		✓	✓	✓	
CVRPLTW	OR-Tools	✓			✓	✓			✓	✓	
OCVRPBTW	OR-Tools	✓			✓	✓		✓	✓		✓
CVRPBLTW	OR-Tools	✓			✓	✓		✓	✓	✓	
OCVRPL	OR-Tools	✓				✓			✓	✓	✓
CVRPBTW	OR-Tools	✓			✓	✓		✓	✓	✓	
OCVRPBL	OR-Tools	✓				✓		✓	✓	✓	✓
OCVRPLTW	OR-Tools	✓			✓	✓		✓	✓	✓	✓
OCVRPBLTW	OR-Tools	✓			✓	✓		✓	✓	✓	✓
CVRPBP	OR-Tools	✓				✓		✓	✓	✓	
OCVRPBP	OR-Tools	✓				✓		✓	✓	✓	✓
CVRPBPL	OR-Tools	✓				✓		✓	✓	✓	
OCVRPBPTW	OR-Tools	✓			✓	✓		✓	✓	✓	✓
CVRPBPLTW	OR-Tools	✓			✓	✓		✓	✓	✓	
CVRPBPTW	OR-Tools	✓			✓	✓		✓	✓	✓	
OCVRPBPL	OR-Tools	✓				✓		✓	✓	✓	✓
OCVRPBPLTW	OR-Tools	✓			✓	✓		✓	✓	✓	✓
MDCVRP	PyVRP	✓				✓			✓	✓	
MDCVRPTW	PyVRP	✓			✓	✓			✓	✓	
MDOCVRP	PyVRP	✓				✓			✓	✓	✓
MDCVRPL	PyVRP	✓				✓			✓	✓	
MDCVRPB	PyVRP	✓				✓		✓	✓	✓	
MDOCVRPTW	PyVRP	✓			✓	✓			✓	✓	✓
MDOCVRPB	PyVRP	✓				✓		✓	✓	✓	✓
MDCVRPBL	PyVRP	✓				✓		✓	✓	✓	
MDCVRPLTW	PyVRP	✓			✓	✓			✓	✓	
MDOCVRPBTW	PyVRP	✓			✓	✓		✓	✓	✓	✓
MDCVRPBLTW	PyVRP	✓			✓	✓		✓	✓	✓	
MDOCVRPL	PyVRP	✓				✓			✓	✓	✓
MDCVRPBTW	PyVRP	✓			✓	✓		✓	✓	✓	
MDOCVRPBL	PyVRP	✓				✓		✓	✓	✓	✓
MDOCVRPLTW	PyVRP	✓			✓	✓			✓	✓	✓
MDOCVRPBLTW	PyVRP	✓			✓	✓		✓	✓	✓	✓
MDCVRPBP	PyVRP	✓				✓		✓	✓	✓	
MDOCVRPBP	PyVRP	✓				✓		✓	✓	✓	✓
MDCVRPBPL	PyVRP	✓				✓		✓	✓	✓	
MDOCVRPBPTW	PyVRP	✓			✓	✓		✓	✓	✓	✓
MDCVRPBPLTW	PyVRP	✓			✓	✓		✓	✓	✓	
MDCVRPBPTW	PyVRP	✓			✓	✓		✓	✓	✓	
MDOCVRPBPL	PyVRP	✓				✓		✓	✓	✓	✓
MDOCVRPBPLTW	PyVRP	✓			✓	✓		✓	✓	✓	✓
SPCTSP	ILS		✓	✓		✓					
PDCVRP	OR-Tools	✓				✓	✓		✓	✓	
OPDCVRP	OR-Tools	✓				✓	✓		✓	✓	✓

Table 9: Problem representations of 52 unseen asymmetric VRP variants for zero-shot generalization.

Problem	Oracle	Demand	Prize	Penalty	Time	Depot	Pickup	Backhaul	Delivery	Sub-routes	Open Route
ACVRPTW	OR-Tools	✓			✓	✓			✓	✓	
AOCVRP	OR-Tools	✓				✓			✓	✓	✓
ACVRPL	OR-Tools	✓				✓			✓	✓	
ACVRPB	OR-Tools	✓				✓		✓	✓	✓	
AOCVRPTW	OR-Tools	✓			✓	✓			✓	✓	✓
AOCVRPB	OR-Tools	✓				✓		✓	✓	✓	✓
ACVRPBL	OR-Tools	✓				✓		✓	✓	✓	
ACVRPLTW	OR-Tools	✓			✓	✓			✓	✓	
AOCVRPBTW	OR-Tools	✓			✓	✓		✓	✓	✓	✓
ACVRPBLTW	OR-Tools	✓			✓	✓		✓	✓	✓	
AOCVRPL	OR-Tools	✓				✓			✓	✓	✓
ACVRPBTW	OR-Tools	✓			✓	✓		✓	✓	✓	
AOCVRPBL	OR-Tools	✓				✓		✓	✓	✓	✓
AOCVRPLTW	OR-Tools	✓			✓	✓			✓	✓	✓
AOCVRPBLTW	OR-Tools	✓			✓	✓		✓	✓	✓	✓
ACVRPBP	OR-Tools	✓				✓		✓	✓	✓	
AOCVRPBP	OR-Tools	✓				✓		✓	✓	✓	✓
ACVRPBPL	OR-Tools	✓				✓		✓	✓	✓	
AOCVRPBTW	OR-Tools	✓			✓	✓		✓	✓	✓	✓
ACVRPBPLTW	OR-Tools	✓			✓	✓		✓	✓	✓	
AOCVRPBPL	OR-Tools	✓				✓		✓	✓	✓	✓
AOCVRPBPLTW	OR-Tools	✓			✓	✓		✓	✓	✓	✓
AMDCVRP	OR-Tools	✓				✓			✓	✓	
AMDCVRPTW	OR-Tools	✓			✓	✓			✓	✓	
AMDCVRP	OR-Tools	✓				✓			✓	✓	✓
AMDCVRPL	OR-Tools	✓				✓			✓	✓	
AMDCVRPB	OR-Tools	✓				✓		✓	✓	✓	
AMDCVRPTW	OR-Tools	✓			✓	✓			✓	✓	✓
AMDCVRPB	OR-Tools	✓				✓		✓	✓	✓	✓
AMDCVRPBL	OR-Tools	✓				✓		✓	✓	✓	
AMDCVRPLTW	OR-Tools	✓			✓	✓			✓	✓	
AMDCVRPBTW	OR-Tools	✓			✓	✓		✓	✓	✓	✓
AMDCVRPBLTW	OR-Tools	✓			✓	✓		✓	✓	✓	
AMDCVRPL	OR-Tools	✓				✓			✓	✓	✓
AMDCVRPBTW	OR-Tools	✓			✓	✓		✓	✓	✓	
AMDCVRPBL	OR-Tools	✓				✓		✓	✓	✓	✓
AMDCVRPLTW	OR-Tools	✓			✓	✓			✓	✓	✓
AMDCVRPBLTW	OR-Tools	✓			✓	✓		✓	✓	✓	✓
AMDCVRPBP	OR-Tools	✓				✓		✓	✓	✓	
AMDCVRPBP	OR-Tools	✓				✓		✓	✓	✓	✓
AMDCVRPBPL	OR-Tools	✓				✓		✓	✓	✓	
AMDCVRPBPBTW	OR-Tools	✓			✓	✓		✓	✓	✓	✓
AMDCVRPBPLTW	OR-Tools	✓			✓	✓		✓	✓	✓	
AMDCVRPBPBTW	OR-Tools	✓			✓	✓		✓	✓	✓	
AMDCVRPBPL	OR-Tools	✓				✓		✓	✓	✓	✓
AMDCVRPBLTW	OR-Tools	✓			✓	✓		✓	✓	✓	✓
APDTSP	OR-Tools					✓	✓		✓		
APDCVRP	OR-Tools	✓				✓	✓		✓	✓	
AOPDCVRP	OR-Tools	✓				✓	✓		✓	✓	✓
AOP	OR-Tools		✓			✓			✓		
APCTSP	OR-Tools		✓	✓		✓			✓		
ASPCTSP	ILS		✓	✓		✓			✓		

G Unified Data Representation

We introduce the UDR $U = \{\mathbf{u}_i\}_{i=0}^n$ to encode each node i into a high-dimensional vector $\mathbf{u}_i = [\Phi(v_i); \boldsymbol{\omega}_i; \boldsymbol{\xi}_i]$. This representation integrates three essential components: a bidirectional Fréchet representation (BFR) $\Phi(v_i)$ to capture directional geometric relationships, a unified attribute set $\boldsymbol{\omega}_i$ to represent local constraints, and a node-type indicator $\boldsymbol{\xi}_i$ to define functional roles.

Building upon Zhou et al. [14], we refine the UDR through two key enhancements. First, we replace the position identifier composed of random identifiers and node coordinates with the proposed unified bidirectional Fréchet representation. Second, we decouple the original Pickup/Backhaul-Deliver/Linehaul structure into two distinct categories: Pickup-Delivery (PD) and Backhaul-Linehaul (BL). This separation is motivated by the fundamental structural differences between the two constraints. Specifically, in PD constraints, pickup and delivery nodes are strictly paired with an explicit precedence relationship. In contrast, the BL relationship primarily serves to distinguish node functionalities: linehaul nodes receive goods from the depot, while backhaul nodes return them, with no direct one-to-one matching between them. Coupling these disparate logic flows into a single representation would impede the model’s convergence and optimization efficiency.

Table 10: Detailed description of each component in UDR.

Attribute Name	Symbol	Range	Description	Examples
BFR	$\Phi(v)$	\mathbb{R}	Normalized bidirectional Fréchet distances to M pivots.	All Variants
Demand	δ	$[-1, 1]$	Node demand (+ for delivery/linehaul, – for pickup/backhaul).	CVRP, PDCVRP
Prize	ϵ	$[0, 1]$	Prize collected for each node.	OP, PCTSP
Penalty	μ	$[0, 1]$	Penalty incurred for each node.	PCTSP
Earliest Arrival Time	e	$[0, 1]$	Earliest permissible arrival time.	CVRPTW
Latest Arrival Time	l	$[0, 1]$	Latest permissible arrival time (deadline).	CVRPTW
Service Time	s	$[0, 1]$	Time required for service at the node.	CVRPTW
Depot	–	$\{0, 1\}$	Indicates if the node is a depot.	CVRP
Pickup Node	–	$\{0, 1\}$	Indicates if the node is a pickup location.	PDTSP, APDTSP
Delivery Node	–	$\{0, 1\}$	Indicates if the node is a delivery location.	PDTSP, APDTSP
Backhaul Node	–	$\{0, 1\}$	Indicates if the node is a backhaul location.	CVRPB, ACVRPB
Linehaul Node	–	$\{0, 1\}$	Indicates if the node is a linehaul location.	CVRPB, ACVRPB
Node in Sub-routes	–	$\{0, 1\}$	The solution π can have sub-routes.	CVRP
Node in Open Route	–	$\{0, 1\}$	Vehicles need not return to the depot.	OCVRP

H Model Architecture and Training

H.1 Embedding Layer

Given an instance \mathcal{G} , we project each component of $\mathbf{u}_i = [\Phi(v_i); \boldsymbol{\omega}_i; \boldsymbol{\xi}_i]$ into a d -dimensional latent space using three independent linear transformations. The initial node embedding $\mathbf{h}_i^{(0)}$ is computed as:

$$\mathbf{h}_i^{(0)} = \Phi(v_i)W_\Phi + \boldsymbol{\omega}_iW_\omega + \boldsymbol{\xi}_iW_\xi, \quad (57)$$

where $W_\Phi \in \mathbb{R}^{2M \times d_h}$, $W_\omega \in \mathbb{R}^{6 \times d_h}$, and $W_\xi \in \mathbb{R}^{7 \times d_h}$ are learnable weight matrices. This process yields a set of initial embeddings $H^{(0)} = \{\mathbf{h}_i^{(0)}\}_{i=0}^n$ for all nodes in \mathcal{G} .

H.2 Encoder

The encoder θ_{enc} consists of L stacked attention layers. It maps initial embeddings $H^{(0)}$ to high-level node representations $H^{(L)} = \{\mathbf{h}_i^{(L)}\}_{i=0}^n$. Each layer contains two primary sub-layers: a Mixed Bias Module (MBM)[14] and a Feed-Forward (FF) network. We integrate both sub-layers using skip-connections and Instance Normalization (IN) [61, 62]. For each layer ℓ , let $H^{(\ell-1)} = \{\mathbf{h}_i^{(\ell-1)}\}_{i=0}^n$ be the input. We compute the intermediate and final outputs for node i as follows:

$$\tilde{\mathbf{h}}_i^{(\ell)} = \text{IN} \left(\mathbf{h}_i^{(\ell-1)} + \text{MBM} \left(\mathbf{h}_i^{(\ell-1)}, H^{(\ell-1)}, \mathbf{D}, \mathbf{D}^T, \mathbf{R} \right) \right), \quad (58)$$

$$\mathbf{h}_i^{(\ell)} = \text{IN} \left(\tilde{\mathbf{h}}_i^{(\ell)} + \text{FF} \left(\tilde{\mathbf{h}}_i^{(\ell)} \right) \right). \quad (59)$$

Here, $\text{MBM}(\cdot)$ denotes the mixed bias module [14], detailed in Equation (63). $\text{FF}(\cdot)$ represents a position-wise feed-forward network with ReLU activation. In addition, we also apply z-score

normalization to \mathbf{D} and \mathbf{D}^T throughout the entire process at SPACE to facilitate gradient flow and accelerate convergence [63].

Mixed Bias Module MBM [14] integrates three structural bias matrices through decoupled attention mechanisms: (1) an outgoing distance matrix \mathbf{D} ; (2) an incoming distance matrix \mathbf{D}^T ; and (3) an optional relation matrix \mathbf{R} . In this module, the relation elements $r_{ij} \in \mathbf{R}$ are set to 0 if a predefined relationship exists (e.g., pickup–delivery pairing) and 1 otherwise. This encoding ensures that smaller values represent higher structural affinities. For the ℓ -th layer, the MBM computes three parallel attention outputs:

$$\bar{\mathbf{h}}_i^{(0)} = \text{Attention}(\mathbf{h}_i^{(\ell-1)}, H^{(\ell-1)}, f(\alpha, N, \mathbf{D}_i)), \quad (60)$$

$$\bar{\mathbf{h}}_i^{(1)} = \text{Attention}(\mathbf{h}_i^{(\ell-1)}, H^{(\ell-1)}, f(\alpha, N, \mathbf{D}_i^T)), \quad (61)$$

$$\bar{\mathbf{h}}_i^{(2)} = \begin{cases} \text{Attention}(\mathbf{h}_i^{(\ell-1)}, H^{(\ell-1)}, f(\alpha, \mathbf{R}_i)) & \text{if } \mathbf{R} \neq \emptyset \\ \mathbf{0} & \text{otherwise,} \end{cases}, \quad (62)$$

The intermediate results are then aggregated via concatenation and a linear projection:

$$\hat{\mathbf{h}}_i^{(\ell)} = [\bar{\mathbf{h}}_i^{(0)}, \bar{\mathbf{h}}_i^{(1)}, \bar{\mathbf{h}}_i^{(2)}] W^O, \quad (63)$$

where $W^O \in \mathbb{R}^{(3 \times d_h) \times d_h}$ is a learnable weight matrix.

For $\text{Attention}(\cdot)$, MBM employs the Adaptation Attention Free Module (AAFM) [9]. This module enhances the model’s sensitivity to diverse geometric patterns via an adaptive function $f(\alpha, N, d_{ij})$ conditioned on a bias weight α . The bias weight α is generated by a lightweight bias network, denoted as $\text{BIAS}(\boldsymbol{\lambda})$, which takes the multi-hot representation $\boldsymbol{\lambda}$ of a sample as input. Formally, the computation is defined as:

$$\text{BIAS}(\boldsymbol{\lambda}) = \max(0, (\boldsymbol{\lambda}W_1 + \mathbf{b}_1)W_2 + \mathbf{b}_2), \quad (64)$$

where $W_1 \in \mathbb{R}^{|\boldsymbol{\lambda}| \times d_h}$, $W_2 \in \mathbb{R}^{d_h \times 1}$, $\mathbf{b}_1 \in \mathbb{R}^{d_h}$, and $\mathbf{b}_2 \in \mathbb{R}^1$ represent the learnable parameters. Consistent with Zhou et al. [14], we omit the scale factor N in the adaptation function for \mathbf{R} , as the relations r_{ij} are inherently scale-independent. In cases where \mathbf{R} is absent, we initialize $\bar{\mathbf{h}}_i^{(2)}$ as a zero vector to maintain structural consistency.

Adaptation Attention Free Module Following Zhou et al. [9], we implement $\text{Attention}(\cdot)$ using an adaptation attention free module (AAFM) to enhance geometric pattern recognition for routing problems. Given the input X , AAFM first transforms it into Q , K , and V through corresponding linear projection operations:

$$Q = XW^Q, \quad K = XW^K, \quad V = XW^V, \quad (65)$$

where W^Q , W^K , and W^V are learnable matrices. The AAFM computation is then expressed as:

$$\text{Attention}(Q, K, V, A) = \sigma(Q) \odot \frac{\exp(A)(\exp(K) \odot V)}{\exp(A) \exp(K)}, \quad (66)$$

where σ denotes the sigmoid function, \odot represents the element-wise product, and $A = \{a_{ij}\}$ denotes the pair-wise adaptation bias. For distance matrices, the corresponding adaptation bias $f(\alpha, N, d_{ij}) = -\alpha \cdot \log_2 N \cdot d_{i,j}$. Here, $N = |\mathcal{V}|$ denotes the total number of nodes (i.e., problem size), and α is generated via a lightweight network $\text{BIAS}(\boldsymbol{\lambda})$ in our paper (see Equation (64)). Notably, for the relation matrix, we remove the scale N in the calculation of adaptation bias because the relation is scale-independent.

Compared to multi-head attention (MHA) [25], AAFM enables the model to explicitly capture instance-specific knowledge by updating pair-wise adaptation biases while exhibiting lower computational overhead.

H.3 Decoder

The decoder constructs a distribution over the next node at each autoregressive step. Since WDAD and AAFM have been defined in Section 3.2, Appendix E, and Equation (66), we only specify how these modules are instantiated inside the decoder. Before decoding, WDAD generates five effective projection matrices conditioned on the multi-hot problem representation λ : two query projections for the first and last selected nodes, $W_{\text{first}}^{Q,(\lambda)}$ and $W_{\text{last}}^{Q,(\lambda)}$, the key and value projections $W^{K,(\lambda)}$ and $W^{V,(\lambda)}$, and the state projection $W^{C,(\lambda)}$. Given the encoded node embeddings $H^{(L)} = \{\mathbf{h}_i^{(L)}\}_{i=0}^n$, the candidate keys and values are cached before decoding:

$$K = H^{(L)}W^{K,(\lambda)}, \quad V = H^{(L)}W^{V,(\lambda)}. \quad (67)$$

At step t , the context query is formed from the first selected node, the most recently selected node, and the optional scalar problem state C_t :

$$\mathbf{q}_t = \mathbf{h}_{\pi_1}^{(L)}W_{\text{first}}^{Q,(\lambda)} + \mathbf{h}_{\pi_{t-1}}^{(L)}W_{\text{last}}^{Q,(\lambda)} + C_tW^{C,(\lambda)}, \quad (68)$$

where $C_t = 0$ for variants that do not require an explicit state signal. The state variables used in SPACE are summarized in the next subsection. Let $\tilde{\mathbf{d}}_t$ denote the z-score normalized outgoing distance vector from the current node to all candidate nodes, and let $\mathcal{M}_t \in \{0, -\infty\}^{n+1}$ denote the feasibility mask introduced in Section 2. Similar to the encoder, the decoder uses two independent instances of the bias network in Equation (64) to produce distance-bias coefficients α_{attn} and α_{com} . The first coefficient defines the AAFM bias for decoder readout:

$$\mathbf{a}_t^{\text{dec}} = -\alpha_{\text{attn}} \log_2 N \cdot \tilde{\mathbf{d}}_t + \mathcal{M}_t, \quad \mathbf{h}'_t = \text{Attention}(\mathbf{q}_t, K, V, \mathbf{a}_t^{\text{dec}}), \quad (69)$$

so infeasible candidates are suppressed within the same four-argument AAFM form used in Equation (66). The updated context \mathbf{h}'_t is then matched against the original encoded node embeddings through a single-head compatibility layer. A second distance bias is added before clipping:

$$\mathbf{s}_t = \frac{\mathbf{h}'_t(H^{(L)})^\top}{\sqrt{d_h}} - \alpha_{\text{com}} \log_2 N \cdot \tilde{\mathbf{d}}_t. \quad (70)$$

Finally, the transition probability is obtained by applying tanh clipping and the feasibility mask:

$$p_\theta(\pi_t = i \mid \pi_{1:t-1}, \mathcal{G}) = \text{Softmax}(\zeta \cdot \tanh(\mathbf{s}_t) + \mathcal{M}_t)_i, \quad (71)$$

where ζ is the logit clipping constant. This decoder preserves the standard autoregressive selection pipeline while allowing the effective projections and distance biases to adapt to the active routing attributes.

H.4 Problem State C_t

In this section, we detail the problems that require additional state signals. For the problem state C_t , we follow the settings in the URS [14], and the specific operations are as follows:

- For all problems with the capacity constraint, we explicitly impose **only remaining load**, while diverse additional constraints (e.g., time windows, duration limit, and backhaul) are enforced implicitly as \mathcal{M}_t masks infeasible candidate nodes to guarantee valid solutions, instead of being fully enumerated in the input of the decoder.
- For (A)OP, we keep track of the remaining maximum length at time t , and C_t represents the remaining routing length that can be moved, and we normalize it to $[0, 1]$ by dividing by the maximum length (i.e., 4.0 in OP100 and 1.0 in AOP100). The setting is the same as AM [21].
- For (A)PCTSP and (A)SPCTSP, C_t is the remaining prize to collect, and we do not provide any information about the penalties, as this is irrelevant for the remaining decisions, following Kool et al. [21].

H.5 Training

To enable the model to better capture features shared across different routing problems, we adopt a per-iteration random problem-type sampling strategy: at each training step, we randomly select one problem from the set of 12 training problems, and randomly generate a mini-batch (128 in our experiment) of instances of that problem for training.

Following Kwon et al. [8], we use n trajectories with distinct starting nodes in training. SPACE is trained by the REINFORCE [29] algorithm with a shared baseline [8]:

$$\nabla_{\theta} \mathcal{L}(\theta) = \mathbb{E}_{p(\pi|\mathcal{G},\theta)}[(f(\pi|\mathcal{G}) - \frac{1}{n} \sum_{i=1}^n f(\pi^i|\mathcal{G})) \nabla_{\theta} \log p_{\theta}(\pi|\mathcal{G})], \quad (72)$$

$$p_{\theta}(\pi | \mathcal{G}) = \prod_{t=2}^n p_{\theta}(\pi_t | \mathcal{G}, \pi_{1:t-1}), \quad (73)$$

where the objective function $f(\pi|\mathcal{G})$ represents the total reward (e.g., the negative value of tour length) of instance \mathcal{G} given a specific solution π .

H.6 Model and Training Hyperparameters

Detailed information on the hyperparameter settings can be found in Table 11. The training of SPACE is conducted on a single NVIDIA GeForce RTX 4090 GPU (24GB of memory). The training procedure requires only about 110 hours (≈ 5 days) in total (500 epochs at approximately 13 minutes each) to obtain a unified parameter set capable of addressing a broad class of routing problems.

Table 11: The hyperparameter settings of SPACE.

Hyperparameter	Value
Optimizer	AdamW
Clipping parameter ζ	50
Initial learning rate	10^{-4}
Epochs of learning rate decay	[451]
Factor of learning rate decay	0.1
Weight decay	10^{-6}
The number of encoder layers	12
Embedding dimension d_h	128
Feed forward dimension	512
Number of Pivots M	8
WDAD Rank r	32
WDAD Heads	3
Training scale	100
Batches of each epoch	2,000
Batch size	128
Training Epochs	500

I Detailed Experimental Results

I.1 Consistent Problem Settings

This section reports the complete per-problem comparison under the same problem settings used in the main experiments. We group the evaluated variants into single-depot and multi-depot families in Tables 12 and 13. For each variant, we report the optimality gap and inference time under both symmetric and asymmetric distance matrices, together with the average gap across the two settings. A dash indicates that the method does not support the corresponding setting. For readability, we list the seen (a)symmetric variants corresponding to unseen variants together if necessary.

For single-depot variants, Table 12 shows that SPACE achieves the lowest average gap on most evaluated problems. Compared with URS, SPACE improves 27 of 31 average gaps, with gains mainly from the asymmetric side while maintaining symmetric performance. The improvement is especially clear in compositional variants that include open routes, backhauls, time windows, and duration limits. URS remains slightly better on a few simpler or prize-collecting cases, indicating that the main benefit of SPACE is not isolated symmetric specialization but robust transfer across symmetric and asymmetric realizations of the same constraint structure.

For multi-depot variants, Table 13 shows a stronger asymmetry-related trend. SPACE obtains lower asymmetric gaps than URS on all 24 multi-depot variants and the lowest average gap on 22 of them. SPACE consistently reduces the degradation caused by asymmetric distances. These results support the role of the proposed unified representation in maintaining stable generalization when both the depot structure and the underlying distance geometry change.

I.2 Inconsistent Problem Settings

For our cross-problem experiment in the main text, RF [30] and CaDA [31] are excluded due to discrepancies in the problems, including the number of training CVRP variants (16 in their work vs. 5 in ours) and constraint settings (i.e., Backhauls and Time Windows). To ensure a fair comparison with RF [30] and CaDA [31], we evaluate SPACE against the official best-performing version of RouteFinder (i.e., RF-TE) and CaDA models on a subset of problems that all three methods have both seen and unseen, strictly filtering for variants where the constraint definitions align perfectly across all methods. As shown in Table 14, when evaluated under strictly matched conditions, SPACE still performs best overall among comparable methods. Note that SPACE can provide the strongest zero-shot generalization across all shared unseen problems.

Table 12: Detailed results on single-depot VRPs.

Method	Symmetric Gap (Time)	Asymmetric Gap (Time)	Average Gap	Symmetric Gap (Time)	Asymmetric Gap (Time)	Average Gap	Symmetric Gap (Time)	Asymmetric Gap (Time)	Average Gap
Problem	CVRPBL			OCVRPBL			OCVRPBLTW		
Oracle	0.00% (3.5h)	0.00% (3.5h)	0.00%	0.00% (3.5h)	0.00% (3.5h)	0.00%	0.00% (3.5h)	0.00% (3.5h)	0.00%
MVMoE	1.35% (12s)	—	—	7.12% (12s)	—	—	10.01% (15s)	—	—
MTPOMO	1.79% (6s)	—	—	7.34% (7s)	—	—	10.50% (7s)	—	—
ReLD-MTL	1.01% (7s)	—	—	5.41% (7s)	—	—	9.22% (8s)	—	—
URS	1.65% (6s)	6.18% (2.4m)	3.92%	9.47% (7s)	17.23% (2.7m)	13.35%	13.72% (8s)	14.32% (2.5m)	14.02%
SPACE	1.67% (6s)	-14.27% (1.8m)	-6.30%	7.36% (7s)	-1.94% (1.8m)	2.71%	11.63% (8s)	5.52% (2.3m)	8.57%
Problem	CVRPBLTW			CVRPBP			CVRPBPL		
Oracle	0.00% (3.5h)	0.00% (3.5h)	0.00%	0.00% (6.6m)	0.00% (6.6m)	0.00%	0.00% (6.6m)	0.00% (6.6m)	0.00%
MVMoE	7.33% (16s)	—	—	13.95% (14s)	—	—	13.38% (14s)	—	—
MTPOMO	7.75% (8s)	—	—	13.71% (7s)	—	—	13.44% (8s)	—	—
ReLD-MTL	6.94% (9s)	—	—	13.57% (9s)	—	—	12.96% (10s)	—	—
URS	9.18% (8s)	10.18% (2.4m)	9.68%	12.95% (7s)	24.20% (2.4m)	18.58%	12.65% (8s)	24.03% (2.6m)	18.34%
SPACE	8.29% (8s)	-0.37% (2.3m)	3.96%	13.49% (8s)	7.93% (2.0m)	10.71%	13.13% (8s)	7.82% (2.2m)	10.47%
Problem	CVRPBPLTW			CVRPBP			OCVRP		
Oracle	0.00% (6.6m)	0.00% (6.6m)	0.00%	0.00% (20.8m)	0.00% (6.6m)	0.00%	0.00% (5.3m)	0.00% (6.6m)	0.00%
MVMoE	16.66% (16s)	—	—	1.28% (11s)	—	—	3.14% (13s)	—	—
MTPOMO	17.15% (10s)	—	—	1.67% (5s)	—	—	3.46% (6s)	—	—
ReLD-MTL	15.95% (12s)	—	—	0.90% (6s)	—	—	2.32% (7s)	—	—
URS	18.33% (10s)	13.82% (2.8m)	16.08%	1.46% (6s)	7.10% (2.1m)	4.28%	3.24% (6s)	37.63% (2.9m)	20.44%
SPACE	17.54% (11s)	4.16% (2.9m)	10.85%	1.45% (6s)	-14.05% (1.7m)	-6.30%	3.31% (7s)	11.18% (1.8m)	7.24%
Problem	CVRPBPTW			CVRPBPTW			CVRPL		
Oracle	0.00% (6.6m)	0.00% (6.6m)	0.00%	0.00% (3.5h)	0.00% (3.5h)	0.00%	0.00% (16m)	0.00% (16m)	0.00%
MVMoE	16.86% (15s)	—	—	7.08% (15s)	—	—	0.26% (12s)	—	—
MTPOMO	17.22% (9s)	—	—	7.41% (7s)	—	—	0.48% (6s)	—	—
ReLD-MTL	16.09% (11s)	—	—	6.74% (8s)	—	—	0.02% (8s)	—	—
URS	18.15% (9s)	14.52% (2.6m)	16.33%	8.94% (8s)	9.95% (2.2m)	9.45%	0.43% (7s)	-2.24% (1.9m)	-0.91%
SPACE	17.57% (10s)	4.73% (2.7m)	11.15%	7.91% (8s)	-0.52% (2.1m)	3.69%	0.45% (7s)	-1.88% (2.0m)	-0.72%
Problem	CVRPLTW			OCVRPBP			OCVRPBPTW		
Oracle	0.00% (3.5h)	0.00% (3.5h)	0.00%	0.00% (3.5h)	0.00% (3.5h)	0.00%	0.00% (6.6m)	0.00% (6.6m)	0.00%
MVMoE	1.47% (16s)	—	—	7.09% (12s)	—	—	9.42% (15s)	—	—
MTPOMO	1.92% (9s)	—	—	7.34% (5s)	—	—	9.94% (9s)	—	—
ReLD-MTL	1.17% (11s)	—	—	5.36% (6s)	—	—	8.43% (11s)	—	—
URS	2.67% (9s)	12.22% (2.7m)	7.45%	9.35% (6s)	18.05% (2.5m)	13.70%	10.05% (8s)	17.45% (2.5m)	13.75%
SPACE	1.82% (9s)	2.26% (2.6m)	2.04%	7.33% (6s)	-1.34% (1.7m)	2.99%	9.62% (9s)	9.65% (2.7m)	9.64%
Problem	OCVRPBP			OCVRPBPL			OCVRPBPLTW		
Oracle	0.00% (6.6m)	0.00% (6.6m)	0.00%	0.00% (6.6m)	0.00% (6.6m)	0.00%	0.00% (6.6m)	0.00% (6.6m)	0.00%
MVMoE	18.27% (14s)	—	—	17.75% (14s)	—	—	8.87% (16s)	—	—
MTPOMO	17.90% (8s)	—	—	17.31% (8s)	—	—	9.47% (10s)	—	—
ReLD-MTL	15.81% (9s)	—	—	15.21% (10s)	—	—	8.06% (11s)	—	—
URS	16.96% (7s)	32.58% (2.5m)	24.77%	16.37% (8s)	32.50% (2.7m)	24.44%	9.51% (9s)	13.82% (2.8m)	11.66%
SPACE	16.85% (8s)	17.40% (2.1m)	17.12%	16.31% (8s)	17.00% (2.3m)	16.66%	9.23% (10s)	8.57% (2.9m)	8.90%
Problem	OCVRPBPTW			OCVRPL			OCVRPLTW		
Oracle	0.00% (3.5h)	0.00% (6.6m)	0.00%	0.00% (3.5h)	0.00% (3.5h)	0.00%	0.00% (3.5h)	0.00% (3.5h)	0.00%
MVMoE	9.95% (15s)	—	—	3.15% (13s)	—	—	3.90% (15s)	—	—
MTPOMO	10.45% (6s)	—	—	3.44% (6s)	—	—	4.37% (8s)	—	—
ReLD-MTL	9.29% (8s)	—	—	2.31% (8s)	—	—	3.16% (9s)	—	—
URS	13.77% (7s)	14.45% (2.3m)	14.11%	3.22% (7s)	37.36% (3.1m)	20.29%	5.12% (9s)	16.35% (2.8m)	10.74%
SPACE	11.60% (7s)	5.48% (2.2m)	8.54%	3.29% (7s)	11.02% (2.0m)	7.15%	4.26% (9s)	6.99% (2.6m)	5.63%
Problem	TSP			OP			PCTSP		
Oracle	0.00% (6m)	0.00% (2m)	0.00%	0.00% (1.5m)	0.00% (6.6m)	0.00%	0.00% (1.2h)	0.00% (6.6m)	0.00%
GOAL-MTL	—	1.77% (1m)	—	1.20% (38s)	—	—	—	—	—
URS	0.57% (6s)	2.26% (1.1m)	1.42%	0.45% (4s)	-5.47% (1.2m)	-2.51%	1.06% (5s)	43.79% (1.2m)	22.43%
SPACE	0.64% (5s)	2.89% (1.4m)	1.77%	0.44% (5s)	-12.13% (1.4m)	-5.85%	0.88% (5s)	73.95% (1.5m)	37.42%
Problem	SPCTSP			PDCVRP			OPDCVRP		
Oracle	—	—	—	0.00% (6.6m)	0.00% (6.6m)	0.00%	0.00% (6.6m)	0.00% (6.6m)	0.00%
URS	-2.37% (5s)	0.00% (1.2m)	-1.19%	-1.47% (4.3s)	7.03% (1.2m)	2.78%	4.93% (4.3s)	11.13% (1.2m)	8.03%
SPACE	-2.60% (5s)	20.05% (1.5m)	8.73%	0.38% (5.1s)	1.26% (1.3m)	0.82%	7.90% (5.4s)	4.60% (1.4m)	6.25%
Problem	CVRP			CVRPTW			OCVRPTW		
Oracle	0.00% (9.1m)	0.00% (6.6m)	0.00%	0.00% (19.6m)	0.00% (6.6m)	0.00%	0.00% (20.8m)	0.00% (6.6m)	0.00%
MVMoE	1.65% (12s)	—	—	4.90% (15s)	—	—	3.85% (15s)	—	—
MTPOMO	1.85% (6s)	—	—	5.31% (8s)	—	—	4.41% (7s)	—	—
ReLD-MTL	1.42% (8s)	—	—	4.56% (10s)	—	—	3.10% (9s)	—	—
GOAL-MTL	4.22% (48s)	—	—	4.66% (42s)	—	—	—	—	—
URS	1.81% (6s)	3.06% (1.4m)	2.44%	6.13% (8s)	11.28% (2.5m)	8.71%	5.07% (8s)	17.47% (2.6m)	11.27%
SPACE	1.83% (7s)	2.67% (1.8m)	2.25%	5.36% (9s)	1.54% (2.4m)	3.45%	4.20% (8s)	7.97% (2.4m)	6.08%
Problem	PDTSP			—			—		
Oracle	0.00% (9.8m)	0.00% (6.6m)	0.00%	—	—	—	—	—	—
URS	4.98% (4s)	6.21% (1.0m)	5.60%	—	—	—	—	—	—
SPACE	4.71% (5s)	-7.46% (1.2m)	-1.38%	—	—	—	—	—	—

Table 13: Detailed results on multi-depot VRPs.

Method	Symmetric Gap (Time)	Asymmetric Gap (Time)	Average Gap	Symmetric Gap (Time)	Asymmetric Gap (Time)	Average Gap	Symmetric Gap (Time)	Asymmetric Gap (Time)	Average Gap
Problem	MDCVRP			MDCVRPB			MDCVRPBL		
Oracle	0.00% (6.6m)	0.00% (6.6m)	0.00%	0.00% (6.6m)	0.00% (6.6m)	0.00%	0.00% (6.6m)	0.00% (6.6m)	0.00%
MVMoE	32.39% (1.8m)	—	—	16.70% (1.5m)	—	—	16.50% (1.5m)	—	—
MTPOMO	27.25% (1.3m)	—	—	13.41% (1.0m)	—	—	11.92% (1.1m)	—	—
ReLD-MTL	18.79% (1.5m)	—	—	7.71% (1.1m)	—	—	6.87% (1.2m)	—	—
URS	12.88% (56s)	4.67% (15m)	8.77%	3.94% (45s)	8.52% (15m)	6.23%	3.12% (48s)	9.66% (15m)	6.39%
SPACE	16.67% (1.0m)	3.93% (15m)	10.30%	5.49% (50s)	-9.40% (12m)	-1.95%	5.00% (53s)	-8.50% (12m)	-1.75%
Problem	MDCVRPBLTW			MDCVRPBP			MDCVRPLTW		
Oracle	0.00% (6.6m)	0.00% (6.6m)	0.00%	0.00% (6.6m)	0.00% (6.6m)	0.00%	0.00% (6.6m)	0.00% (6.6m)	0.00%
MVMoE	50.63% (1.8m)	—	—	62.05% (2.0m)	—	—	41.51% (2.1m)	—	—
MTPOMO	42.54% (1.3m)	—	—	52.27% (1.4m)	—	—	34.21% (1.5m)	—	—
ReLD-MTL	35.33% (1.5m)	—	—	38.98% (1.6m)	—	—	26.44% (1.8m)	—	—
URS	36.76% (1.0m)	13.18% (18m)	24.97%	31.19% (1.0m)	27.10% (20m)	29.14%	32.92% (1.3m)	15.26% (22m)	24.09%
SPACE	35.97% (1.1m)	2.70% (18m)	19.33%	34.16% (1.2m)	9.69% (17m)	21.92%	27.29% (1.3m)	4.64% (21m)	15.97%
Problem	MDOCVRPBL			MDCVRPBPBL			MDCVRPBLTW		
Oracle	0.00% (6.6m)	0.00% (6.6m)	0.00%	0.00% (6.6m)	0.00% (6.6m)	0.00%	0.00% (6.6m)	0.00% (6.6m)	0.00%
MVMoE	29.70% (1.6m)	—	—	62.41% (2.1m)	—	—	56.55% (2.3m)	—	—
MTPOMO	24.25% (1.1m)	—	—	52.77% (1.4m)	—	—	47.00% (1.7m)	—	—
ReLD-MTL	17.33% (1.2m)	—	—	38.79% (1.6m)	—	—	40.18% (2.0m)	—	—
URS	13.29% (49s)	25.18% (17m)	19.24%	30.76% (1.1m)	25.81% (20m)	28.28%	37.99% (1.4m)	17.16% (23m)	27.58%
SPACE	12.95% (49s)	10.31% (13m)	11.63%	34.20% (1.2m)	8.66% (17m)	21.43%	39.38% (1.5m)	7.51% (23m)	23.44%
Problem	MDCVRPBTW			MDCVRPBTW			MDCVRPL		
Oracle	0.00% (6.6m)	0.00% (6.6m)	0.00%	0.00% (6.6m)	0.00% (6.6m)	0.00%	0.00% (6.6m)	0.00% (6.6m)	0.00%
MVMoE	56.76% (2.3m)	—	—	51.68% (1.7m)	—	—	32.23% (1.9m)	—	—
MTPOMO	46.92% (1.6m)	—	—	43.01% (1.2m)	—	—	27.94% (1.3m)	—	—
ReLD-MTL	40.02% (2.0m)	—	—	35.21% (1.5m)	—	—	19.29% (1.5m)	—	—
URS	38.11% (1.3m)	17.94% (23m)	28.03%	36.51% (1.0m)	13.29% (18m)	24.90%	13.05% (58s)	3.94% (15m)	8.49%
SPACE	39.88% (1.4m)	8.22% (21m)	24.05%	36.79% (1.1m)	2.69% (17m)	19.74%	16.76% (1.1m)	3.46% (15m)	10.11%
Problem	MDOCVRPBLTW			MDOCVRPBP			MDOCVRPBL		
Oracle	0.00% (6.6m)	0.00% (6.6m)	0.00%	0.00% (6.6m)	0.00% (6.6m)	0.00%	0.00% (6.6m)	0.00% (6.6m)	0.00%
MVMoE	46.31% (1.8m)	—	—	60.72% (2.1m)	—	—	60.87% (2.1m)	—	—
MTPOMO	39.03% (1.3m)	—	—	48.33% (1.5m)	—	—	47.56% (1.5m)	—	—
ReLD-MTL	33.71% (1.6m)	—	—	36.09% (1.7m)	—	—	36.15% (1.7m)	—	—
URS	29.49% (1.0m)	21.24% (17m)	25.36%	24.97% (1.1m)	37.37% (22m)	31.17%	24.99% (1.1m)	36.71% (22m)	30.85%
SPACE	26.37% (1.0m)	14.34% (17m)	20.36%	27.64% (1.1m)	23.35% (17m)	25.49%	27.79% (1.1m)	22.81% (17m)	25.30%
Problem	MDCVRPTW			MDOCVRP			MDOCVRPB		
Oracle	0.00% (6.6m)	0.00% (6.6m)	0.00%	0.00% (6.6m)	0.00% (6.6m)	0.00%	0.00% (6.6m)	0.00% (6.6m)	0.00%
MVMoE	40.61% (2.1m)	—	—	37.43% (1.9m)	—	—	29.77% (1.5m)	—	—
MTPOMO	33.05% (1.5m)	—	—	29.65% (1.3m)	—	—	24.80% (1.1m)	—	—
ReLD-MTL	25.48% (1.8m)	—	—	22.86% (1.5m)	—	—	17.66% (1.2m)	—	—
URS	31.51% (1.3m)	15.38% (21m)	23.45%	17.63% (57s)	42.04% (22m)	29.84%	13.46% (47s)	25.95% (16m)	19.70%
SPACE	25.97% (1.2m)	4.73% (19m)	15.35%	15.01% (1.0m)	22.11% (15m)	18.56%	13.07% (47s)	11.03% (12m)	12.05%
Problem	MDOCVRPBLTW			MDOCVRPBTW			MDOCVRPTW		
Oracle	0.00% (6.6m)	0.00% (6.6m)	0.00%	0.00% (6.6m)	0.00% (6.6m)	0.00%	0.00% (6.6m)	0.00% (6.6m)	0.00%
MVMoE	48.64% (2.3m)	—	—	49.11% (2.3m)	—	—	35.99% (2.1m)	—	—
MTPOMO	40.66% (1.6m)	—	—	41.05% (1.6m)	—	—	30.29% (1.4m)	—	—
ReLD-MTL	36.80% (2.1m)	—	—	36.87% (2.0m)	—	—	24.87% (1.8m)	—	—
URS	26.84% (1.3m)	22.06% (22m)	24.45%	26.88% (1.3m)	23.22% (21m)	25.05%	22.05% (1.1m)	25.30% (20m)	23.67%
SPACE	25.46% (1.3m)	16.08% (21m)	20.77%	25.19% (1.3m)	16.98% (21m)	21.09%	18.21% (1.1m)	16.29% (19m)	17.25%
Problem	MDOCVRPBTW			MDOCVRPL			MDOCVRPLTW		
Oracle	0.00% (6.6m)	0.00% (6.6m)	0.00%	0.00% (6.6m)	0.00% (6.6m)	0.00%	0.00% (6.6m)	0.00% (6.6m)	0.00%
MVMoE	46.75% (1.8m)	—	—	37.48% (2.0m)	—	—	35.82% (2.1m)	—	—
MTPOMO	39.07% (1.2m)	—	—	29.37% (1.4m)	—	—	30.08% (1.5m)	—	—
ReLD-MTL	33.68% (1.5m)	—	—	22.87% (1.6m)	—	—	24.65% (1.8m)	—	—
URS	29.54% (58s)	21.97% (17m)	25.75%	17.64% (1.0m)	42.56% (23m)	30.10%	21.88% (1.1m)	24.30% (20m)	23.09%
SPACE	26.52% (59s)	15.16% (18m)	20.84%	15.08% (1.0m)	22.46% (16m)	18.77%	18.16% (1.1m)	15.35% (20m)	16.75%

Table 14: Comparison with RF and CaDA on shared seen and unseen VRP variants.

Method	Seen		Unseen				Avg.gap	Best Sol.
	CVRP	OCVRP	MDCVRP	MDOCVRP	MDCVRPL	MDOCVRPL		
RF-TE	2.06%	2.86%	63.60%	33.52%	66.75%	34.40%	33.86%	0/6
CaDA	2.17%	2.80%	40.96%	53.21%	42.40%	53.34%	32.48%	1/6
SPACE	1.83%	3.31%	16.67%	15.01%	16.76%	15.08%	11.44%	5/6

J Results On Benchmark Dataset

We provide detailed results on public CVRPLIB benchmark instances in this section. CVRPLIB Set-X [32] and Set-XXL [33] contain fixed large-scale real-world instances with hundreds to thousands of nodes. Since all neural solvers are trained only on generated instances of size $N = 100$, this benchmark evaluates whether the learned routing policy generalizes to substantially larger instances.

Table 15 reports the detailed Set-X results with $N \in [500, 1000]$. SPACE achieves the lowest average gap among the compared neural solvers. These results indicate that the proposed SPACE not only improves performance on synthetic training-scale distributions but also strengthens the transfer of a generalist neural solver to established large-scale benchmark instances.

Table 15: Results on large-scale CVRPLIB instances (Set-X) [32] ($N \in [500, 1000]$).

Set-X Instance	Opt.	POMO-MTL		MVMoE/4E		MVMoE/4E-L		RF-MVMoE		RF-TE		CaDA		ReLD-MTL		URS		SPACE	
		Obj.	Gap	Obj.	Gap	Obj.	Gap	Obj.	Gap	Obj.	Gap	Obj.	Gap	Obj.	Gap	Obj.	Gap	Obj.	Gap
X-n502-k39	69226	77284	11.640%	73533	6.222%	74429	7.516%	76338	10.274%	71791	3.705%	189318	173.478%	71954	3.941%	71281	2.969%	74139	7.097%
X-n513-k21	24201	28510	17.805%	32102	32.647%	31231	29.048%	32639	34.866%	28465	17.619%	236328	876.522%	27554	13.855%	26166	8.119%	26311	8.719%
X-n524-k153	154593	192249	24.358%	186540	20.665%	182392	17.982%	170999	10.612%	174381	12.800%	226478	46.500%	171465	10.914%	175250	13.362%	176153	13.946%
X-n536-k96	94846	106514	12.302%	109581	15.536%	108543	14.441%	105847	11.599%	103272	8.884%	203165	114.205%	101259	6.761%	102969	8.564%	103115	8.718%
X-n548-k50	86700	94562	9.068%	95894	10.604%	95917	10.631%	104289	20.287%	100956	16.443%	220653	154.502%	91802	5.885%	89768	3.539%	90421	4.292%
X-n561-k42	42717	47846	12.007%	56008	31.114%	51810	21.287%	53383	24.969%	49454	15.771%	288552	575.497%	47390	10.939%	45964	7.601%	45681	6.939%
X-n573-k30	50673	60913	20.208%	59473	17.366%	57042	12.569%	61524	21.414%	55952	10.418%	144633	185.424%	53893	6.354%	54361	7.278%	54880	8.302%
X-n586-k159	190316	208893	9.761%	215668	13.321%	214577	12.748%	212151	11.473%	205575	8.018%	319620	67.942%	202742	6.529%	202645	6.478%	201504	5.879%
X-n599-k92	108451	120333	10.956%	128949	18.901%	125279	15.517%	126578	16.714%	116560	7.477%	224439	106.950%	116539	7.458%	114423	5.507%	114959	6.001%
X-n613-k62	59535	67984	14.192%	82586	38.718%	74945	25.884%	73456	23.383%	67267	12.987%	348589	485.519%	65896	10.684%	65901	10.693%	63680	6.962%
X-n627-k43	62164	73060	17.528%	70987	14.193%	70905	14.061%	70414	13.271%	67572	8.700%	148241	138.468%	67329	8.309%	66499	6.973%	66889	7.601%
X-n641-k35	63682	72643	14.071%	75329	18.289%	72655	14.090%	71975	13.023%	70831	11.226%	423415	564.890%	69382	8.951%	67005	5.218%	67369	5.790%
X-n655-k131	106780	116988	9.560%	117678	10.206%	118475	10.952%	119057	11.497%	112202	5.078%	161519	51.263%	110656	3.630%	110237	3.237%	109203	2.269%
X-n670-k130	146332	190118	29.922%	197695	35.100%	183447	25.364%	168226	14.962%	168999	15.490%	274207	87.387%	167064	14.168%	184010	25.748%	170270	16.359%
X-n685-k75	68205	80892	18.601%	97388	42.787%	89441	31.136%	82269	20.620%	77847	14.137%	342170	401.679%	75501	10.697%	75942	11.344%	74776	9.634%
X-n701-k44	81923	92075	12.392%	98469	20.197%	94924	15.870%	90189	10.090%	89932	9.776%	397296	384.963%	88989	8.625%	86038	5.023%	86556	5.655%
X-n716-k35	43373	52709	21.525%	56773	30.895%	52305	20.593%	52250	20.467%	49669	14.516%	229530	429.200%	48602	12.056%	46496	7.200%	46320	6.795%
X-n733-k159	136187	161961	18.925%	178322	30.939%	167477	22.976%	156387	14.833%	148463	9.014%	289794	112.791%	147574	8.361%	147743	8.485%	145816	7.070%
X-n749-k98	77269	90582	17.229%	100438	29.985%	94497	22.296%	92147	19.255%	85171	10.227%	191170	147.408%	84643	9.543%	83759	8.399%	83278	7.777%
X-n766-k71	114417	144041	25.891%	152352	33.155%	136255	19.086%	130505	14.061%	129935	13.563%	297390	159.918%	126834	10.852%	139371	21.810%	127186	11.160%
X-n783-k48	72386	83169	14.897%	100383	38.677%	92960	28.423%	96336	33.087%	83185	14.919%	532247	635.290%	81305	12.321%	77437	6.978%	78570	8.543%
X-n801-k40	73305	85077	16.059%	91560	24.903%	87662	19.585%	87118	18.843%	86164	17.542%	595083	711.790%	81063	10.583%	77369	5.544%	77933	6.313%
X-n819-k171	158121	177157	12.039%	183599	16.113%	185832	17.525%	179596	13.581%	174441	10.321%	385566	143.842%	169248	7.037%	171024	8.160%	170592	7.887%
X-n837-k142	193737	214207	10.566%	229526	18.473%	221286	14.220%	230362	18.904%	208528	7.635%	393693	103.210%	206963	6.827%	203457	5.017%	203379	4.977%
X-n856-k95	88965	101774	14.398%	99129	11.425%	106816	20.065%	105801	18.924%	98291	10.483%	480248	439.817%	96215	8.149%	94547	6.274%	96288	8.231%
X-n876-k59	99299	116617	17.440%	119619	20.463%	114333	15.140%	114016	14.821%	107416	8.174%	501455	404.995%	105900	6.648%	105417	6.161%	104368	5.105%
X-n895-k37	53860	65587	21.773%	79018	46.710%	64310	19.402%	69099	28.294%	64871	20.444%	597118	1008.648%	62970	16.914%	58137	7.941%	58511	8.635%
X-n916-k207	329179	361719	9.885%	383681	16.557%	374016	13.621%	373600	13.494%	352998	7.236%	619583	88.221%	350310	6.419%	346556	5.279%	346431	5.241%
X-n936-k151	132715	186262	40.347%	220926	66.466%	190407	43.471%	161343	21.571%	163162	22.942%	388590	192.800%	155144	16.900%	172675	30.110%	157340	18.555%
X-n957-k87	85465	98198	14.898%	113882	33.250%	105629	23.593%	123633	44.659%	102689	20.153%	414723	385.255%	93156	9.999%	90485	5.874%	90710	6.137%
X-n979-k58	118976	138092	16.067%	146347	23.005%	139682	17.404%	131754	10.740%	129952	9.225%	542553	356.019%	127584	7.235%	125353	5.360%	125495	5.479%
X-n1001-k43	72355	87660	21.153%	114448	58.176%	94734	30.929%	88969	22.962%	85929	18.760%	781780	980.478%	83572	15.503%	77739	7.441%	79256	9.538%
Avg. Gap		16.796%		26.408%		19.607%		18.795%		12.303%		334.840%		9.439%		8.678%		7.863%	

Table 16 further evaluates the more challenging Set-XXL instances with $N \in [3000, 7000]$. Most neural baselines cannot handle large instances due to memory limitations. Combined with the Set-X results, SPACE achieves the lowest benchmark average across all reported size ranges, supporting its robustness under out-of-distribution scale transfer.

Table 16: Results on large-scale CVRPLIB instances (Set-XXL) [33] ($N \in [3000, 7000]$).

Method	Leuven1 (N=3000)	Leuven2 (N=4000)	Antwerp1 (N=6000)	Antwerp2 (N=7000)	Avg.gap
MTPOMO	67.72%	87.31%	OOM	OOM	—
MVMoE/4E	299.10%	170.10%	OOM	OOM	—
MVMoE/4E-L	182.28%	127.07%	OOM	OOM	—
RF-MVMoE	57.30%	160.27%	OOM	OOM	—
RF-TE	26.90%	45.56%	OOM	OOM	—
CaDA	1035.51%	OOM	OOM	OOM	—
ReLD-MTL	17.00%	30.59%	OOM	OOM	—
URS	11.57%	17.80%	9.23%	14.95%	13.39%
SPACE	8.79%	16.26%	7.82%	15.69%	12.14%

K Training Problem Selection

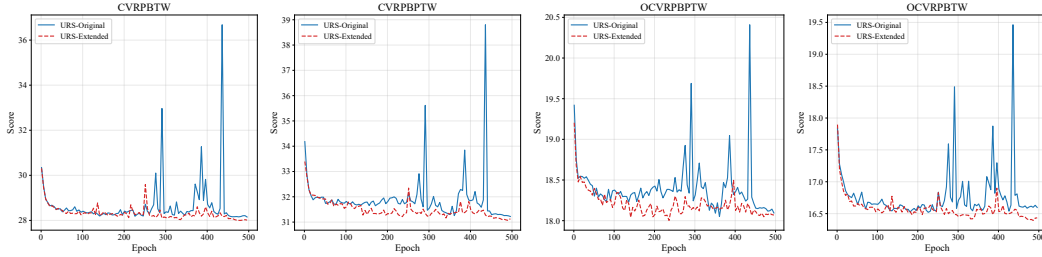


Figure 3: The validation curves of URS trained w/o ACVRPBTW (denoted as URS-Original) and w. ACVRPBTW (denoted as URS-Extended).

As detailed in Section 4, our training set encompasses 12 VRP variants. Unlike the URS configuration, we include ACVRPBTW in our training set. This design choice is driven by two primary considerations: (1) As discussed in Appendix G and F, SPACE enhances the original UDR by replacing the random identifier and node coordinate indicators with our bidirectional Fréchet representation. This architectural update requires the model to learn unified routing knowledge from symmetric and asymmetric variants. Given that the original URS incorporates only two asymmetric problems (i.e., ATSP and ACVRP), we deliberately introduce an additional asymmetric variant to enhance the model’s representational learning capacity. (2) More importantly, since SPACE is built from the architecture of URS, as empirically observed in Figure 3, the original URS exhibits severe performance instability on variants containing both B and TW constraints. We find that including this specific problem effectively stabilizes training on these complex variants that integrate B and TW constraints.

The main paper compares against URS under its published training protocol, because this corresponds to the official baseline and keeps the primary comparison aligned with prior work. To ensure a fair comparison, we conduct a controlled comparison by retraining a URS variant (denoted URS-Extended) on the same 12 training problems as SPACE. This setting directly tests whether improvements in SPACE can be explained by differences in training problems. To have a comprehensive experimental comparison, we evaluate SPACE against URS-Extended on 96 VRPs (48 CVRP variants and their asymmetric counterparts). As shown in Tables 17 and 18, SPACE still achieves lower average gaps under the matched training set compared to URS-Extended. Notably, our SPACE achieves better results across substantially more variants. These results indicate that the gains mainly come from the proposed unified representation and adaptive decoding, rather than from increased training problems.

Table 17: Controlled comparison on symmetric variants with URS retrained on the same training problems as SPACE.

Method	CVRPTW	OCVRP	CVRPL	CVRPB	OCVRPTW
URS-Extended	5.78%	3.28%	0.45%	1.47%	4.79%
SPACE	5.36%	3.31%	0.45%	1.45%	4.20%
Method	OCVRPB	CVRPBL	CVRPLTW	OCVRPBTW	CVRPBLTW
URS-Extended	8.42%	1.68%	2.30%	12.45%	8.63%
SPACE	7.33%	1.67%	1.82%	11.60%	8.29%
Method	OCVRPL	CVRPBTW	OCVRPBL	OCVRPLTW	OCVRPBLTW
URS-Extended	3.25%	8.27%	8.54%	4.84%	12.52%
SPACE	3.29%	7.91%	7.36%	4.26%	11.63%
Method	CVRPBP	OCVRPBP	CVRPBL	OCVRPBTW	CVRPBLTW
URS-Extended	13.74%	17.41%	13.20%	9.72%	17.62%
SPACE	13.49%	16.85%	13.13%	9.62%	17.54%
Method	CVRPBTW	OCVRPBL	OCVRPBLTW	CVRP	MDCVRPTW
URS-Extended	17.61%	16.60%	9.22%	1.83%	30.86%
SPACE	17.57%	16.31%	9.23%	1.83%	25.97%
Method	MDOCVRP	MDCVRPL	MDCVRPB	MDOCVRPTW	MDOCVRPB
URS-Extended	16.80%	18.31%	3.97%	22.22%	13.53%
SPACE	15.01%	16.76%	5.49%	18.21%	13.07%
Method	MDCVRPBL	MDCVRPLTW	MDOCVRPTW	MDCVRPBLTW	MDOCVRPL
URS-Extended	3.32%	32.77%	29.22%	37.92%	16.61%
SPACE	5.00%	27.29%	26.52%	35.97%	15.08%
Method	MDCVRPBTW	MDOCVRPL	MDOCVRPLTW	MDOCVRPTW	MDCVRPBP
URS-Extended	38.17%	13.36%	22.50%	29.30%	31.31%
SPACE	36.79%	12.95%	18.16%	26.37%	34.16%
Method	MDOCVRBP	MDCVRPBL	MDOCVRPTW	MDCVRPBLTW	MDCVRPBTW
URS-Extended	26.88%	31.00%	27.03%	39.52%	39.77%
SPACE	27.63%	34.20%	25.19%	39.38%	39.88%
Method	MDOCVRPL	MDOCVRPTW	MDCVRP	Avg.gap	Best Sol.
URS-Extended	26.80%	27.58%	17.95%	16.67%	10/48
SPACE	27.79%	25.45%	16.67%	15.93%	38/48

Table 18: Controlled comparison on asymmetric variants with URS retrained on the same training problems as SPACE.

Method	ACVRPTW	AOCVRP	ACVRPL	ACVRPB	AOCVRPTW
URS-Extended	1.84%	26.82%	-2.23%	-14.45%	14.06%
SPACE	1.54%	11.18%	-1.88%	-14.05%	7.97%
Method	AOCVRPB	ACVRPBL	ACVRPLTW	AOCVRPBTW	ACVRPBLTW
URS-Extended	10.97%	-14.77%	2.62%	7.88%	0.20%
SPACE	-1.34%	-14.27%	2.26%	5.48%	-0.37%
Method	AOCVRPL	ACVRPBTW	AOCVRPBL	AOCVRPLTW	AOCVRPBLTW
URS-Extended	26.98%	0.07%	10.74%	12.95%	7.96%
SPACE	11.02%	-0.52%	-1.94%	6.99%	5.52%
Method	ACVRPBP	AOCVRPBP	ACVRPBPB	AOCVRPBPB	ACVRPBPB
URS-Extended	8.00%	27.20%	7.82%	11.99%	4.69%
SPACE	7.93%	17.40%	7.82%	9.65%	4.16%
Method	ACVRPBPB	AOCVRPBPB	AOCVRPBPB	ACVRP	AMDCVRPTW
URS-Extended	5.34%	26.87%	10.88%	-1.96%	6.88%
SPACE	4.73%	17.00%	8.57%	-1.62%	4.72%
Method	AMDCVRP	AMDCVRPL	AMDCVRPB	AMDCVRPTW	AMDCVRPB
URS-Extended	32.08%	4.23%	-9.89%	25.00%	16.09%
SPACE	22.11%	3.46%	-9.40%	16.29%	11.03%
Method	AMDCVRPBL	AMDCVRPLTW	AMDCVRPBTW	AMDCVRPBLTW	AMDCVRPL
URS-Extended	-8.84%	6.55%	19.19%	5.87%	32.23%
SPACE	-8.50%	4.64%	15.16%	2.70%	22.46%
Method	AMDCVRPBTW	AMDCVRPBL	AMDCVRPLTW	AMDCVRPBLTW	AMDCVRPBP
URS-Extended	5.82%	15.59%	24.31%	18.31%	11.38%
SPACE	2.69%	10.31%	15.35%	14.34%	9.69%
Method	AMDCVRPBP	AMDCVRPBPB	AMDCVRPBPB	AMDCVRPBPB	AMDCVRPBPB
URS-Extended	28.24%	10.49%	21.18%	11.50%	11.93%
SPACE	23.35%	8.66%	16.98%	7.51%	8.22%
Method	AMDCVRPBPB	AMDCVRPBPB	AMDCVRP	Avg.gap	Best Sol.
URS-Extended	27.82%	20.07%	4.94%	11.20%	6/48
SPACE	22.81%	16.08%	3.93%	7.13%	42/48

L Ablation Study

L.1 Effects of Bidirectional Fréchet Representation

Table 19 reports the per-variant ablation results for the main BFR design components. *Pivot* indicates whether the BFR is used; when disabled, the model falls back to a unified representation (e.g., GOAL). *FPS* indicates whether pivots are selected by Furthest Pivot Sampling; when disabled, pivots are selected randomly. *Depot* indicates whether the depot is used as the initial pivot; when disabled, the initial pivot is randomly selected. *Bi.* indicates whether both incoming and outgoing pivot distances are retained; when disabled, they are replaced by their bidirectional average.

The complete BFR design achieves the best average gap in both symmetric and asymmetric settings. Removing the entire BFR increases the symmetric average gap, showing that BFR provides useful representation beyond other unified representations. Among the individual components, FPS is the most important: replacing FPS with random pivot selection increases the average gap to 83.10% on symmetric variants and 95.72% on asymmetric variants. This confirms that BFR depends not only on using pivots, but also on selecting spatially diverse pivots that cover the topology. Removing depot initialization or bidirectional coordinates leads to smaller but consistent degradation, indicating that the depot anchor and direction-aware coordinates further stabilize the representation.

Table 19: Detailed ablation results for Bidirectional Fréchet Representation.

Pivot	FPS	depot	Bi.	CVRP	CVRPTW	OCVRP	CVRPL	CVRPB	OCVRPTW
×	×	×	×	2.25%	6.33%	4.00%	0.91%	2.21%	5.47%
✓	×	✓	✓	23.23%	37.06%	121.75%	21.01%	26.24%	177.45%
✓	✓	×	✓	2.09%	5.77%	3.51%	0.68%	1.81%	4.61%
✓	✓	✓	×	1.92%	5.55%	3.58%	0.54%	1.66%	4.42%
✓	✓	✓	✓	1.83%	5.36%	3.31%	0.45%	1.45%	4.20%
Pivot	FPS	depot	Bi.	OCVRPB	OCVRPL	CVRPBL	CVRPBTW	CVRPLTW	OCVRPBL
×	×	×	×	9.69%	4.02%	2.43%	9.52%	2.84%	9.77%
✓	×	✓	✓	88.19%	120.92%	25.43%	31.31%	32.60%	88.03%
✓	✓	×	✓	7.54%	3.48%	2.08%	9.62%	2.25%	7.69%
✓	✓	✓	×	7.99%	3.61%	1.90%	9.42%	2.02%	8.17%
✓	✓	✓	✓	7.33%	3.29%	1.67%	7.91%	1.82%	7.36%
Pivot	FPS	depot	Bi.	OCVRPBTW	OCVRPLTW	CVRPBLTW	OCVRPBLTW	Avg.gap	Best Sol.
×	×	×	×	23.94%	5.58%	9.76%	23.98%	7.67%	0/16
✓	×	✓	✓	164.07%	177.23%	31.71%	163.39%	83.10%	0/16
✓	✓	×	✓	13.81%	4.67%	10.08%	13.94%	5.85%	0/16
✓	✓	✓	×	13.81%	4.49%	9.87%	13.80%	5.80%	0/16
✓	✓	✓	✓	11.60%	4.26%	8.29%	11.63%	5.11%	16/16
Pivot	FPS	depot	Bi.	ACVRP	ACVRPTW	AOCVRP	ACVRPL	ACVRPB	AOCVRPTW
×	×	×	×	4.15%	3.75%	10.66%	-0.48%	-13.37%	10.65%
✓	×	✓	✓	123.94%	59.05%	161.50%	111.28%	92.95%	86.93%
✓	✓	×	✓	2.79%	2.24%	10.46%	-1.75%	-12.77%	9.25%
✓	✓	✓	×	3.90%	2.78%	15.43%	-0.76%	-14.12%	9.27%
✓	✓	✓	✓	2.67%	1.54%	11.18%	-1.88%	-14.05%	7.97%
Pivot	FPS	depot	Bi.	AOCVRPB	AOCVRPL	ACVRPBL	ACVRPBTW	ACVRPLTW	AOCVRPBL
×	×	×	×	-1.50%	10.50%	-13.61%	0.87%	4.53%	-2.09%
✓	×	✓	✓	132.02%	162.44%	82.90%	48.48%	60.47%	127.58%
✓	✓	×	✓	1.20%	10.41%	-13.01%	-0.36%	2.98%	0.40%
✓	✓	✓	×	0.95%	15.30%	-14.42%	0.04%	3.60%	0.45%
✓	✓	✓	✓	-1.34%	11.02%	-14.27%	-0.52%	2.26%	-1.94%
Pivot	FPS	depot	Bi.	AOCVRPBTW	AOCVRPLTW	ACVRPBLTW	AOCVRPBLTW	Avg.gap	Best Sol.
×	×	×	×	6.73%	9.71%	1.01%	6.63%	2.38%	2/16
✓	×	✓	✓	73.04%	86.95%	49.25%	72.75%	95.72%	0/16
✓	✓	×	✓	6.50%	8.26%	-0.17%	6.52%	2.06%	2/16
✓	✓	✓	×	5.69%	8.38%	0.16%	5.65%	2.64%	2/16
✓	✓	✓	✓	5.48%	6.99%	-0.37%	5.52%	1.27%	10/16

L.2 Effects of Pivot Set Size

Table 20 studies the sensitivity of BFR to the number of pivots M . The default setting $M = 8$ achieves the best average gap in both symmetric and asymmetric settings, respectively. Using fewer pivots ($M = 5$) remains competitive on symmetric variants but provides less stable asymmetric transfer. Increasing the pivot count beyond 8 does not improve performance: larger values, such as $M = 20$ or $M = 30$, can introduce redundant or noisy reference-distance coordinates and increase the input dimensionality. Overall, $M = 8$ provides the best trade-off between geometric coverage and representation compactness.

Table 20: Detailed ablation results for the number of pivots in BFR.

Pivot	CVRP	CVRPTW	OCVRP	CVRPL	CVRPB	OCVRPTW
5	1.84%	5.29%	3.32%	0.47%	1.42%	4.25%
10	1.92%	5.50%	3.23%	0.53%	1.62%	4.29%
20	2.09%	5.74%	3.49%	0.67%	1.80%	4.71%
30	2.16%	5.67%	3.60%	0.76%	1.89%	4.50%
8	1.83%	5.36%	3.31%	0.45%	1.45%	4.20%

Pivot	OCVRPB	OCVRPL	CVRPBL	CVRPBTW	CVRPLTW	OCVRPBL
5	7.31%	3.29%	1.57%	8.27%	1.74%	7.35%
10	7.50%	3.26%	1.80%	8.96%	1.99%	7.70%
20	7.91%	3.43%	2.07%	9.46%	2.32%	7.91%
30	7.89%	3.59%	2.14%	9.08%	2.18%	8.06%
8	7.33%	3.29%	1.67%	7.91%	1.82%	7.36%

Pivot	OCVRPBTW	OCVRPLTW	CVRPBLTW	OCVRPBLTW	Avg.gap	Best Sol.
5	11.92%	4.35%	8.65%	11.92%	5.19%	6/16
10	12.94%	4.39%	9.35%	13.00%	5.50%	2/16
20	13.54%	4.79%	9.81%	13.51%	5.83%	0/16
30	12.83%	4.66%	9.39%	12.73%	5.70%	0/16
8	11.60%	4.26%	8.29%	11.63%	5.11%	8/16

Pivot	ACVRP	ACVRPTW	AOCVRP	ACVRPL	ACVRPB	AOCVRPTW
5	2.99%	2.02%	12.15%	-1.61%	-13.05%	8.89%
10	2.73%	2.08%	13.56%	-1.85%	-14.02%	10.94%
20	2.97%	1.97%	10.81%	-1.53%	-15.21%	8.86%
30	2.80%	1.86%	16.93%	-1.73%	-14.67%	9.11%
8	2.67%	1.54%	11.18%	-1.88%	-14.05%	7.97%

Pivot	AOCVRPB	AOCVRPL	ACVRPBL	ACVRPBTW	ACVRPLTW	AOCVRPBL
5	0.64%	11.89%	-13.26%	-0.31%	2.74%	-0.06%
10	1.36%	13.47%	-14.27%	-0.46%	2.79%	0.74%
20	-0.38%	10.66%	-15.43%	-0.17%	2.76%	-1.02%
30	1.91%	16.93%	-15.00%	-0.14%	2.64%	1.32%
8	-1.34%	11.02%	-14.27%	-0.52%	2.26%	-1.94%

Pivot	AOCVRPBTW	AOCVRPLTW	ACVRPBLTW	AOCVRPBLTW	Avg.gap	Best Sol.
5	5.88%	7.97%	-0.16%	5.94%	2.04%	0/16
10	5.46%	10.04%	-0.31%	5.37%	2.35%	1/16
20	6.11%	8.08%	-0.04%	6.13%	1.54%	4/16
30	5.34%	8.25%	-0.03%	5.38%	2.55%	1/16
8	5.48%	6.99%	-0.37%	5.52%	1.27%	10/16

L.3 Effects of Weight-Decomposed Adaptive Decoding

Table 21 reports the per-variant ablation results for WDAD. In the *WDAD* column, \times replaces WDAD with the original URS hypernetwork. The value 1 denotes the single-head ablation under the same total adapter rank budget as the multi-head setting, and 3 denotes the default $H = 3$ WDAD configuration.

The comparison shows that BFR alone is not sufficient; the decoder also needs a parameterization that separates geometry-invariant routing knowledge from constraint-conditioned decision logic. When WDAD is replaced by the URS-style hypernetwork, the adaptive projections are generated from the problem representation as a whole, so routing attributes can be coupled again with metric-specific patterns observed during training. In contrast, WDAD forms each effective decoder weight as $W_{\text{eff}}^{(\lambda)} = W_0 + \Delta W^{(\lambda)}$, where the shared base weight W_0 carries reusable geometric decoding behavior and $\Delta W^{(\lambda)}$ is the average of active attribute-specific updates. This additive mean aggregation keeps the update scale stable when multiple constraints coexist and makes an unseen variant behave more like a composition of learned constraint primitives, especially when asymmetric distances alter pairwise costs and constraint-induced feasibility while the constraint primitives should remain reusable.

The single-head variant further indicates that the improvement is not solely due to the addition of a low-rank adapter. Although it uses the same total rank budget, a single normalized update direction per attribute tends to merge heterogeneous effects into one residual pathway. The multi-head decomposition instead lets each routing attribute express several complementary directions with independent row-wise magnitudes, so the decoder can adapt its query, key, value, and state projections without allowing any single constraint to dominate the effective weight scale. The consistent advantage of the default setting, therefore, supports the intended role of WDAD: separating geometry-invariant decoding from constraint-conditioned decision adjustments and enabling smoother transfer to unseen constraint combinations.

Table 21: Detailed ablation results for Weight-Decomposed Adaptive Decoding.

WDAD	CVRP	CVRPTW	OCVRP	CVRPL	CVRPB	OCVRPTW
\times	2.04%	6.02%	3.70%	0.68%	2.04%	5.21%
1	1.98%	5.61%	3.61%	0.61%	1.76%	4.48%
3	1.83%	5.36%	3.31%	0.45%	1.45%	4.20%
WDAD	OCVRPB	OCVRPL	CVRPBL	CVRPBTW	CVRPLTW	OCVRPBL
\times	11.81%	3.63%	2.27%	10.67%	2.50%	11.92%
1	8.16%	3.59%	2.02%	8.55%	2.11%	8.33%
3	7.33%	3.29%	1.67%	7.91%	1.82%	7.36%
WDAD	OCVRPBTW	OCVRPLTW	CVRPBLTW	OCVRPBLTW	Avg.gap	Best Sol.
\times	17.15%	5.36%	10.85%	17.11%	7.06%	0/16
1	12.58%	4.53%	8.83%	12.60%	5.58%	0/16
3	11.60%	4.26%	8.29%	11.63%	5.11%	16/16
WDAD	ACVRP	ACVRPTW	AOCVRP	ACVRPL	ACVRPB	AOCVRPTW
\times	3.46%	2.72%	16.70%	-1.09%	-13.01%	12.79%
1	2.94%	1.81%	13.09%	-1.67%	-14.65%	9.80%
3	2.67%	1.54%	11.18%	-1.88%	-14.05%	7.97%
WDAD	AOCVRPB	AOCVRPL	ACVRPBL	ACVRPBTW	ACVRPLTW	AOCVRPBL
\times	2.51%	16.39%	-13.27%	0.42%	3.50%	1.91%
1	1.01%	12.85%	-14.93%	-0.22%	2.56%	0.40%
3	-1.34%	11.02%	-14.27%	-0.52%	2.26%	-1.94%
WDAD	AOCVRPBTW	AOCVRPLTW	ACVRPBLTW	AOCVRPBLTW	Avg.gap	Best Sol.
\times	7.93%	11.72%	0.54%	7.91%	3.82%	0/16
1	6.94%	8.97%	-0.08%	6.84%	2.23%	2/16
3	5.48%	6.99%	-0.37%	5.52%	1.27%	14/16

M Licenses For Used Resources

Table 22: List of licenses for the codes and datasets we used in this work.

Resource	Type	Link	License
HGS-PyVRP [59]	Code	https://github.com/PyVRP/PyVRP	MIT License
LKH3 [2]	Code	http://webhotel4.ruc.dk/~keld/research/LKH-3/	Available for academic research use
OR-Tools [60]	Code	https://github.com/google/or-tools	Apache-2.0 License
MTPOMO [10]	Code	https://github.com/FeiLiu36/MTNCO	MIT License
MVMoE [11]	Code	https://github.com/RoyalSkye/Routing-MVMoE	MIT License
RouteFinder [30]	Code	https://github.com/ai4co/routefinder	MIT License
CaDA [31]	Code	https://github.com/CIAM-Group/CaDA	MIT License
ReLD [22]	Code	https://github.com/ziweileonhuang/reld-nco	MIT License
GOAL [13]	Code	https://github.com/naver/goal-co	Available for any non-commercial use
URS [14]	Code	https://github.com/CIAM-Group/URS	MIT License
CVRPLIB Set-X [32]	Dataset	http://vrp.galgos.inf.puc-rio.br/index.php/en/	Available for academic research use
CVRPLIB Set-XXL [33]	Dataset	http://vrp.galgos.inf.puc-rio.br/index.php/en/	Available for academic research use

We list the existing codes and datasets in Table 22, all of which are open-source resources for academic use.

N Broader Impacts

This paper presents work aimed at advancing neural combinatorial optimization for vehicle routing problems. By unifying symmetric and asymmetric VRPs within a generalist neural routing solver, SPACE may reduce the need to design and retrain specialized models for each routing variant, thereby improving the adaptability of learning-based solvers in logistics, supply-chain management, and urban delivery scenarios. More efficient, transferable route-optimization methods could reduce operational costs, travel distance, and energy consumption when deployed with appropriate domain constraints. The proposed method has no potential negative societal impacts that we feel must be specifically highlighted.